



Journal of Surface Mount Technology

Volume 37, Issue 2, 2024

- 2 Novel Method of Incorporating CNT into Additive Manufacturing Electronics Dielectric Material
by Daniel Slep, Ph.D. and Fan Yang, Ph.D., *ChemCubed*
- 6 Condition Monitoring System: A Flexible Hybrid Electronics Approach for Sealed Container Applications
by M. Panahi, A. J. Hanson, D. Maddipatla, S. Masihi, B. J. Bazuin, M. Z. Atashbar, *Western Michigan University*; B. B. Narakathu, *SafeSense Technologies, L.L.C.*; S. Miller, *NextFlex National Manufacturing Institute*
- 19 Intermetallic Compounds in Solder Alloys: Common Misconceptions
by Dave Hillman, *Hillman Electronic Assembly Solutions, LLC*; Tim Pearson, *Collins Aerospace*; Richard Coyle, *Nokia*
- 35 *Corporate Members*



Journal of Surface Mount Technology

June 2024 | Volume 37, Issue 2

ISSN: 1093-7358

6600 City W Parkway, Suite 300

Eden Prairie, MN 55344, USA

Phone: +1 952-920-7682

journal@smta.org

www.smta.org

Editor/Journal Committee Chair

Srinivas Chada, Ph.D.

General Dynamics

Publisher

Mike Konrad

Aqueous Technologies

Production

Ryan Flaherty

Isabel Brown

SMTA

JOURNAL REVIEW COMMITTEE

Kola Akinade, Ph.D.

Cisco Systems, Inc. (Retired)

Prasad Godavarti, Ph.D.

Blue Origin

Babak Arfaei, Ph.D.

Binghamton University

David Hillman

Collins Aerospace (Retired)

Raiyomand Aspandiar, Ph.D.

Intel Corporation

Amol Kane

SLB

Nilesh Badwe, Ph.D.

IIT Kanpur

Pradeep Lall, Ph.D.

Auburn University

Tom Borkes

The Jefferson Project

Tae-Kyu Lee, Ph.D.

Cisco Systems

Rich Brooks

Spartronics

Stephan Meschter, Ph.D.

BAE Systems

Jean-Paul Clech, Ph.D.

EPSI, Inc.

Luu Nguyen, Ph.D.

Psi Quantum

Richard Coyle, Ph.D.

Nokia Bell Labs

Anthony Primavera

Micro Systems Engineering

Gary Freedman

Colab Engineering, LLC

Viswam Puligandla, Ph.D.

Nokia (Retired)

Reza Gaffarian, Ph.D.

Jet Propulsion Laboratory

Paul Vianco, Ph.D.

*Sandia National Laboratories
(Retired)*

COMMITTEE MISSION STATEMENT

The mission of the SMTA Journal Committee is to select and review papers for publication in the Journal of SMT, ensuring a high standard of quality for each issue and ensuring article content best serves SMTA membership.

Summer is heating up and to stay in theme, here is the next issue hot off the presses. Enjoy it with a cold beverage of choice by the pool side or in the comfort of A/C in the house.

Firstly, I'd like to extend a warm welcome to our newest member of the Journal Review Committee, Stephan Meschter, Ph.D. Thank you for supporting this publication. We look forward to your contributions to improve the quality of articles published in future issues.

As always, we bring you three interesting technical articles in this edition. The first paper explores a novel method to improve properties of flexible hybrid electronics that are additively manufactured and incorporating carbon nano tubes. We follow that with an application-oriented paper, wherein two different flexible hybrid electronics are compared for monitoring temperature withing storage containers. The final paper summarizes the effect of intermetallic compounds (IMC) on solder joint reliability from various solder compositions.

This Journal is dependent on excellent publications submitted by our members. To keep up the high technical standards consider sending original papers for review. Remember, the only charge associated with publication is your hard work and intellect unlike several other journals that levy a per page fee.

Lastly, please don't forget to register and attend 2024 SMTA International Conference & Exposition to be held in Rosemont, IL from October 21 to 24.

— *Srini Chada, Ph.D.*

The Journal of SMT Editor/Journal Committee Chair

SUBMIT ORIGINAL PAPERS FOR REVIEW:

1. Go to <https://journal.smta.org> and click "Register"
2. Complete the form to create your profile in the system
3. Once your profile is active, click "Make a Submission"
4. Read all requirements and begin the 5-step process:
 - a. Acknowledge and accept the requirements
 - b. Upload your paper
 - c. Enter metadata
 - d. Confirm your submission
 - e. Review next steps of the process

Contact Ryan Flaherty with questions: ryan@smta.org

ABOUT THE JOURNAL OF SMT

The Journal of SMT is a quarterly, peer-reviewed, technical publication of articles related to electronic assembly technologies, including microsystems, emerging technologies, and related business operations.

Novel Method of Incorporating CNT into Additive Manufacturing Electronics Dielectric Material

Daniel Slep, Ph.D. and Fan Yang, Ph.D.

ChemCubed
Stony Brook, NY, USA

ABSTRACT

Flexible Hybrid Electronics (FHE) Parts that are additively manufactured give engineers and designers greater flexibility in geometry, complexity, and variety or customizability. In this work, UV curable dielectric materials for additive electronics and incorporated Carbon Nano Tubes (CNTs) within a formulated UV/LED curable matrix was used. It will be shown that inkjet printing CNT mixture in specific manner with a commercial UV curable dielectric improves mechanical and thermal properties of the final dielectric compared to the dielectric without the CNT mixture, including a significant decrease in the coefficient of thermal expansion, while keeping excellent electrical properties.

Key words: Dielectric, PCB, FHE, AME, CNT

INTRODUCTION

Printing electronics is a new and quickly growing alternative to traditionally manufactured electronics wherein an additive method is used to produce electronic circuits, passive circuitry, displays, sensors, and radio-frequency identification (RFID) tags utilizing conductive and sometimes dielectric materials. Numerous advances have been made in electronic printing technology in recent years bringing it closer to scalable manufacturing.[1-3] New and faster printing equipment has been engineered and modified for printing electronic traces using conductive inks rather than using copper etching on flexible and rigid substrates.[4,5] Flexible PCBs (FPCB) provide the same processing capability as a standard PCB, with added flexibility, and are better suited for large scale manufacturing applications. FPCB's are more reliable, can bend without breaking/sustaining damage, can withstand greater stress and harsher conditions, and can be adapted to smaller spaces due to thin copper and insulating layers.

If the PCB industry were able to produce complex multilayer circuitry quickly and easily without etching copper and without the numerous hands-on multi-lamination steps thus required, not only would this facilitate the design process, leading to quicker innovation, but it would revolutionize and tremendously enhance production, in

addition to lowering manufacturing costs (especially for low volume production). Achieving this goal provides new functionality to electronics such as incorporation of printed passive electronics to be printed within the layers, reducing the total components placed on a circuit board. Designers could consider these added abilities in designs to increase the complexity of multilayer circuitry utilizing less space. This will allow manufacturers the capability to design and develop circuitry quickly and efficiently.

Widespread adoption of additive manufacturing (AM) has the potential to disrupt current production and supply chains, simplifying these processes, and moving manufacturing capacity closer to the consumer. Rather than an extensive network of storing and shipping parts, parts can be produced on site according to demand. Flexible Hybrid Electronics (FHE) Parts that are 3D printed give engineers and designers greater flexibility in geometry, complexity, and variety or customizability. With traditional manufacturing techniques there is a direct connection between degree of complexity and cost of production. Additive manufacturing eliminates the extra cost burden of additional complexity. Printing discontinued parts, across all industries, also reduces waste and extends the life of various electronics, tools, and machines. Printing electronics gives the user the ability to change designs immediately on the production line, and to design and create previously impossible objects. Additive manufacturing also has significant associated medical impacts. [6-8] Implants, prosthetics, hearing aids, and dental devices can be custom 3D printed. The impact of the technology developed and tested within this work is wide-reaching across several target gap areas including, but not limited to: improvements in materials for multilayer printing, specialized printed components, achieving high levels of performability and robust results. There is extensive overlap in the applicability of the materials and print systems tested in this work and marketability to a solve a variety of needs in the medical, automotive, aerospace, military and commercial manufacturing sectors.

One of the key advances in recent years in AM electronics has been in the conductive inks for inkjet printing. This advance is a main reason why scalable printed manufacture PCBs is now within reach.

Advances with reactive, particle-free silver conductive inks have proven to have high performance and reliability in inkjet applications.

The environmental benefits of additive manufacturing are even greater for printed electronics.[9] This printing method allows for more automation and less hands-on cleaning and heat laminating - also reducing energy. It will enable new designs of energy efficient smart sensors, IoT, and packaging materials.

In addition, there are many applications for FHE/PCB's in the aerospace industry, such as wearable electronics, RFID antennas, satellite communications, navigation and passive detection systems, radio communications, LED lighting systems, temperature sensors, power converters, control tower systems, IOT devices, and others. Furthermore, lack of a secure and domestic supply chain for PCBs poses a national security risk. Increasing the additive manufacturing of PCB boards domestically is critical to enabling the U.S. to manufacture technologically sophisticated devices within our supply chains. Because AM allows PCBs to be manufactured sustainably, economically, and in an environmentally-friendly manner, AM is the conduit for secure and sustainable domestic production.

Despite the technological advances and significant benefits of FHE's, (including, AM PCBs & FPCBs) further R&D is needed to develop materials suited to the conditions of various manufacturing environments and needs. The work here further addresses these needs by showing a method of improved printed dielectric materials using inkjet as the deposition method.

Carbon nanotubes (CNTs) are tubes made of carbon with diameters typically measured in nanometers. CNTs can be chemically modified, and have exceptional tensile strength and thermal conductivity because of their nanostructure and the strength of the bonds between carbon atoms. It has been shown that it is possible to improve mechanical and thermal properties of a polymer matrix by mixing small fraction 1-3% of CNTs into the formula.[10-12] Current use of nanotubes has mostly been limited to the use of bulk nanotubes, which is a mass of unorganized fragments of nanotubes.

In this work, UV curable dielectric materials for additive electronics and incorporating CNTs within a formulated UV/LED curable matrix was used. CNT within a formulated UV/LED curable matrix has been used to make a functional printable dielectric material to show improved performance. Specialized functionalized/dispersed and patented CNT dispersions from Molecular Rebar Design LLC were used.

PROCEDURE

Multilayer circuitry is based on depositing a conductive (usually inorganic) material and a dielectric or insulating material. Some of the challenges in printing multilayer circuitry are that materials (a) must stand up to reflow soldering and (b) have a variety of precise mechanical, thermal, and electronic qualities. Inkjet printing is emerging as having potential for printing FHEs. Inkjet can print digitally-encoded data captured from images and accurately deposit a conductive ink for the traces and pads, and dielectric ink for the solder mask or other advanced statistical machine translation (SMT)

systems. Inkjet deposits dielectric ink between layers of circuitry leaving vias between the layers to be filled with conductive ink. Inkjet also allows the printing of unique identifiers, such as text or a bar code with a serial number within a single platform. These capabilities make inkjet the obvious choice for FHE manufacturing.

For this work, an inkjet system branded ElectroJet which includes dielectric materials and printing equipment capable of printing multi-materials in layers was used and shown in Figure 1.

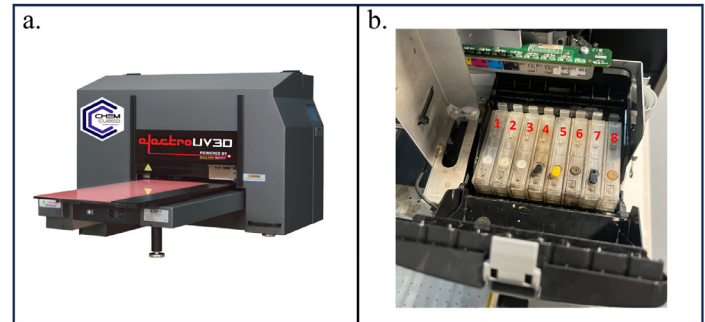


Figure 1: ElectroUV3D printer used in the ElectroJet printing system (a), and it's 8 channels with an individual cartridge dedicated to each channel (b).

Materials

One dielectric material to be used in this work is ChemCubed's Electrojet C3-DI-7 ink with a dielectric constant(ϵ_r) of approximately 3.5, deformation resistance, has electrical insulating properties, and be able to withstand thermal fluctuation from 20oC to 140oC. Another dielectric material, which has <1% multi-walled carbon nanotubes (MWCNTs) with an average length of 900 nm dispersed in compatible UV formulations, is labeled as C3-DI-CNT. The viscosity of C3-DI-7 and C3-DI-CNT is between 5 and 7 cPs.

Printing

ChemCubed has employed a novel printing technique (U.S. Provisional Patent Application Serial No. 63/327,884) to incorporate the nanotube solution into the dielectric. Instead of composing a singular solution with CNT's, ChemCubed prints the dielectric at the same time as the CNT solution causing mixing before curing. The C3-DI-7 and C3-DI-CNT were loaded in different channels within the same printhead of an inkjet printer. An UV LED light was aligned next to the printhead which lighted up while printing. For non-CNT dielectric samples, only the channel contained C3-DI-7 was used. For CNT dielectric samples, C3-DI-7 and C3-DI-CNT channels were being printed simultaneously, resulting in a 1:1 mix ratio of the two materials. The prints were than labelled as C3-DI-7-CNT. The samples were printed and cured layer by layer until a desired thickness was reached. Figure 2 shows a block diagram of the setup of the printhead and how the CNT samples were being printed. Examples of the printed samples can be found in Figure 3.

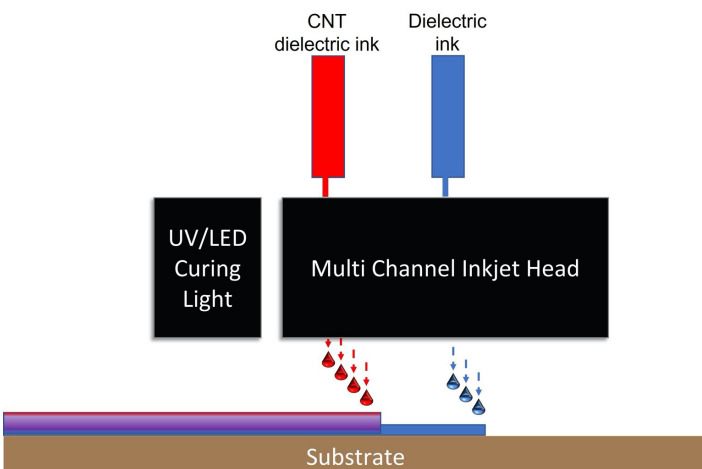


Figure 2: Block diagram of the setup of the printhead.



Figure 3: Examples of printed materials (D = 36 mm). Left: C3-DI-7. Right: C3-DI-7-CNT (mix of C3-DI-7 and C3-DI-CNT).

Testing

Samples has been printed for testing different properties according to corresponding ASTM standards, if possible. Type IV samples in ASTM D638 were used for obtaining Young's modulus, elongation, and tensile strength. The dielectric constant was measured using disk electrodes referenced from ASTM D150 with an electrode diameter of 25 mm. The dielectric strength was measured using a withstand voltage tester with the samples printed in sheets. The glass transition temperature (T_g) and melting point (T_m) were obtained by Differential Scanning Calorimetry (DSC). The thermal conductivity was measured using ASTM E1530 standard by a thermal conductivity meter. The coefficient of thermal expansion (CTE) was obtained by Dynamic Mechanical Analysis (DMA).

RESULTS AND DISCUSSION

Mechanical Properties

The mechanical properties of the electric material were dramatically increased after CNT has been incorporated into the system. As shown in Table 1, both Young's modulus and tensile strength of the CNT dielectric material, C3-DI-CNT, increased by more than 100% compared to the non-CNT one, to be specific, 123.3% and 112.4%, respectively. The results indicate that the CNTs has been successfully well distributed in the dielectric material which reinforced the system with their strong mechanical properties. It also reveals a high bonding strength between the CNT and the dielectric material.

Table 1: Mechanical properties of C3-DI-7 and C3-DI-7-CNT.

	C3-DI-7	C3-DI-7-CNT
Young's modulus (MPa)	300	670
Tensile strength (MPa)	25.8	54.8

Thermal Properties

Table 2 summarizes the thermal properties of the dielectric materials which includes glass transition temperature (T_g), coefficient of thermal expansion (CTE), melting point (T_m), and thermal conductivity. From the table we can find that C3-DI-7 has two separate T_g values, which are around the T_g of its two main components, indicating a separation of polymer blocks. On the contrary, only one T_g was found on C3-DI-7-CNT. This is exciting since CNT not only increased the mechanical properties of the material, but also made it more uniform. Moreover, there was a dramatic decrease in CTE resulting in an over 2.5-fold difference. This is very important since large CTE leads to delamination either when printed on top of other materials or used as substrates. CNT, in this case, "stitched" the dielectric material and prevented it from having a large deformation when heated up. Nevertheless, a 10.3% increase in T_m and a 11.8% increase in thermal conductivity were observed indicating a better thermal stability.

Table 2: Thermal properties of C3-DI-7 and C3-DI-7-CNT.

	C3-DI-7	C3-DI-7-CNT
Glass transition temperature ($^{\circ}\text{C}$)	69, 121	112.7
Coefficient of thermal expansion (1/K)	232	90
T_m , melting point ($^{\circ}\text{C}$)	268.5	296.2
Thermal conductivity (W/mK)	0.17	0.19

Electrical Properties

As dielectric materials, both C3-DI-7 and C3-DI-7-CNT exhibited good electrical properties with dielectric constants of 3.5 and 4.1, respectively. An excellent dielectric strength greater than 50 MV/m was measured on both materials as well.

To have a clearer view of the comparison, a bar graph was plotted in Figure 4 with the property values of C3-DI-7-CNT normalized to the values of C3-DI-7.

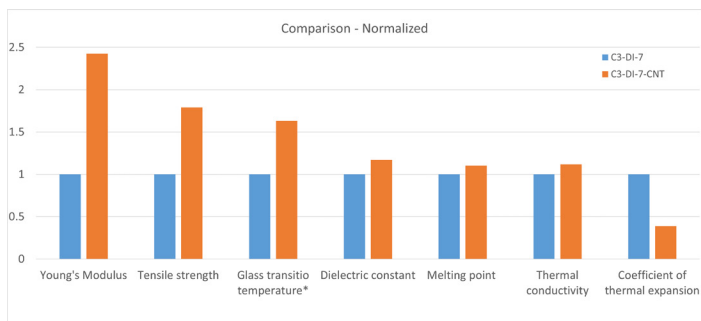


Figure 4: Comparison of different properties with C3-DI-7-CNT values normalized to that of C3-DI-7. *The lower glass transition temperature of C3-DI-7 was used here when compared to C3-DI-7-CNT.

CONCLUSION

In conclusion, we have successfully developed a method for adding CNTs to our dielectric material. The result CNT dielectric material, compared to the original one, showed a great improvement in mechanical and thermal properties while keeping excellent electrical properties.

The proposed mechanism is such that, by laying down a thin film, the nanotubes align themselves in the x-y plane. This causes a strong layering structure. There will be a few nanotubes on surfaces of each layer that would help with the interfaces in the z- direction, almost like stitching the layers. The tubes must be singular, maximizing surface area to have the desired effect. If they agglomerate or bunch up, they will have the opposite effect, and make the material weaker. This new revolutionary printable nanocomposite that will change the way circuits will be designed and manufactured.

ACKNOWLEDGEMENTS

This research was supported in part by a SBIR Phase 1 NIST Award # 70NANB21H062.

The authors would like to thank Clive P. Bosnyak, PhD Cofounder & Chief Technology Officer of Molecular Rebar Design LLC for specially making the CNT dilutions used.

REFERENCES

- [1] Yang, Hui, Wan Ru Leow, and Xiaodong Chen. "3D printing of flexible electronic devices." *Small Methods* 2.1 (2018): 1700259.
- [2] Wei, Peiqi, et al. "Flexible and stretchable electronic skin with high durability and shock resistance via embedded 3D printing technology for human activity monitoring and personal healthcare." *Advanced Materials Technologies* 4.9 (2019): 1900315.
- [3] Zhang, Li, et al. "Research Progress of Microtransfer Printing Technology for Flexible Electronic Integrated Manufacturing." *Micromachines* 12.11 (2021): 1358.
- [4] Cai, Yaguo, et al. "Inkjet printing of particle-free silver conductive ink with low sintering temperature on flexible substrates." *Chemical Physics Letters* 737 (2019): 136857.
- [5] Hong, Hong, Jiyong Hu, and Xiong Yan. "UV curable conductive ink for the fabrication of textile-based conductive circuits and wearable UHF RFID tags." *ACS applied materials & interfaces* 11.30 (2019): 27318-27326.

[6] Culmone, Costanza, Gerwin Smit, and Paul Breedveld. "Additive manufacturing of medical instruments: A state-of-the-art review." *Additive Manufacturing* 27 (2019): 461-473.

[7] Haleem, Abid, and Mohd Javaid. "3D printed medical parts with different materials using additive manufacturing." *Clinical Epidemiology and Global Health* 8.1 (2020): 215-223.

[8] Sinha, Sudip Kumar. "Additive manufacturing (AM) of medical devices and scaffolds for tissue engineering based on 3D and 4D printing." *3D and 4D printing of polymer nanocomposite materials*. Elsevier, 2020. 119-160.

[9] Dong, Yue, Chao Bao, and Woo Soo Kim. "Sustainable additive manufacturing of printed circuit boards." *Joule* 2.4 (2018): 579-582.

[10] Qian, D., et al. "Load transfer and deformation mechanisms in carbon nanotube-polystyrene composites." *Applied physics letters* 76.20 (2000): 2868-2870.

[11] Allaoui, Aissa, et al. "Mechanical and electrical properties of a MWNT/epoxy composite." *Composites science and technology* 62.15 (2002): 1993-1998.

[12] Spindler-Ranta, Sean, and Charles E. Bakis. "Carbon nanotube reinforcement of a filament winding resin." *International SAMPE Symposium and Exhibition (Proceedings)*. Vol. 47. Soc. for the Advancement of Material and Process Engineering, 2002.

BIOGRAPHIES



Dr. Daniel Slep serves as chief executive officer for ChemCubed. Dan's background includes leading manufacturing, research and product development. In these positions, Dan has worked with multiple companies from startups to fortune 500s. Dan has served on multiple External Advisory Boards such as Rutgers Leading Disruptive Innovation and for Chemical Engineering at Stony Brook University. He lectures about topics such as Additive Manufacturing, Polymer Engineering and Nanotechnology. Dan's education includes a bachelor's degree in physics, as well as a master's degree and Doctor of Philosophy in material sciences. During his more than three decades in the printing Industry, Dan has published industry-related articles and scientific papers and is the inventor of multiple patents.



Dr. Fan Yang received his PhD and master's degree in Materials Science and Engineering from Stony Brook University. His research experience involves characterization of materials, modification of polymers, synthesis of nanoparticles, as well as experience in cell biology and developing biomaterials where he has numerous publications in leading scientific journals. Dr. Yang did his post-doctoral work at Stony Brook University. His experience with nanoparticles and polymer materials is a perfect fit for the ongoing research areas at ChemCubed

Condition Monitoring System: A Flexible Hybrid Electronics Approach for Sealed Container Applications

M. Panahi¹, A. J. Hanson^{1,2}, D. Maddipatla¹, S. Masihi¹, B. B. Narakathu², B. J. Bazuin¹, S. Miller³, M. Z. Atashbar¹

¹*Department of Electrical and Computer Engineering, Western Michigan University
Kalamazoo, MI, USA*

²*SafeSense Technologies, L.L.C.
Kalamazoo, MI, USA*

³*NextFlex National Manufacturing Institute
San Jose, CA, USA*

ABSTRACT

A comparative study is presented between two advanced flexible hybrid electronics (FHE) monitoring systems designed for accurately measuring temperature within storage containers across various industries, including food, pharmaceuticals, agriculture, automotive, and defense. Flexible hybrid electronics involve the combination of novel printing processes and traditional electronic manufacturing processes, resulting in flexible devices with improved performance. The first system, a copper-flex system (CFS), employs an 88.9 μm polyimide substrate with 35 μm thick copper traces, coated with a 12.5 μm polyimide solder mask. The second system, a printed-flex system (PFS), utilizes a 127 μm polyimide substrate and screen-printed conductive silver ink. Both FHE systems use a 32-pin very thin quad flat no-lead (VQFN) package attached on a thin polyimide flexible substrate with high-temperature resistance and high-tensile strength. In both CFS and PFS, the VQFN is attached using Sn96.5/Ag3.0/Cu0.5 and Sn42/Bi57.6/Ag0.4 solders, respectively, from Chip Quik® (Ancaster, Ontario, Canada). After assembly, reliability and durability tests were conducted to validate the performance of the temperature sensor and the interconnections of the CFS and PFS prototypes. Further, environmental and mechanical characterizations including, moisture and insulation resistance, corrosion, elongation, bending, terminal bond strength, and peel tests were performed based on IPC-TM-650 and ASTM standards. Moisture and insulation resistance test on the PFS test coupons without a coating layer indicated stable resistance of approximately 18 M Ω , while permanent color change indicated oxidation of copper on uncoated CFS test coupons. After 72 hours of corrosion test, both the CFS and PFS “meander line” test coupons covered with polyimide showed negligible weight and resistance change of approximately 0.35%, and 0%, respectively. A Young’s modulus of 7.17 GPa and 2.6 GPa was calculated from the elongation test for the CFS and PFS, respectively. Bending

tests on PFS revealed negligible average resistance change (0.1%) during 180° bending cycles, while no impact was recorded on the CFS system. During the terminal bond strength test, soldered wires detached from the CFS test coupons at an average force of 43 N, while it was 3.8 N on the PFS test coupons. Both systems with polyimide coating layer demonstrate robustness and reliability for diverse applications in various industries.

Key words: Temperature sensor; asset monitoring system; copper flexible system; printed flexible system; flexible hybrid electronics.

INTRODUCTION

Condition monitoring of tangible assets often entails the utilization of a hardware and software system that records, transmits, stores, and processes information on ambient conditions by using various sensors, data communication technologies, and software algorithms. Condition monitoring systems have found widespread applications across various industries, including automotive, defense, food, and medical industries, for several decades [1-5]. However, the full potential of such systems remains largely untapped in applications that necessitate miniaturized and conformal structures with flexible and thin form factors.

For instance, in agricultural storage applications, there is a need for flexible and lightweight condition monitoring systems to monitor the moisture, temperature, and other environmental conditions of seeds and plants [6]. One other example of a condition monitoring application is in healthcare and logistics. Asset monitoring systems can track the location and condition of vaccine storage containers during transportation. This helps pharmaceutical industries optimize logistics operations and prevent damage or loss of vaccines. For example, during the COVID-19 pandemic, Pfizer-BioNTech produced large quantities of vaccines that had to be transported and stored worldwide at temperatures between 2 °C to 8 °C for up to a month [7].

In addition to vaccines and perishable food items like meat and fruit [8], the US Department of Defense (DoD) emphasizes the importance of condition monitoring for ammunition in a thin and flexible form factor [9]. Precise temperature monitoring during transportation and storage, either long or short-term, is vital to maintain the effectiveness of sensitive items. Temperature changes can result in vaccine wastage, food spoilage, ammunition degradation, or even fatalities, underscoring the need for continuous and accurate condition monitoring. Traditional monitoring systems are often rigid and made using electronic fabrication techniques. However, the market needs lightweight, compact, thin, affordable, and flexible monitoring systems tailored to various applications, especially for monitoring conditions inside containers. Therefore, developing such systems is crucial for the global economy and public health, as they ensure the safe condition of assets in different types of containers.

Flexible hybrid electronics involve the combination of novel printing processes and traditional electronic manufacturing processes, resulting in flexible devices with improved performance [10-22]. In this work, two advanced FHE based condition monitoring systems are designed and fabricated for monitoring temperature inside a DoD-relevant ammunition container (M2A2). A comparative study is performed between a CFS and PFS prototype, which are both based on popular manufacturing processes in FHE. The systems were designed to meet the DoD accepted requirements, in terms of performance and dimension [9]. The capability of the CFS and PFS were tested to monitor temperature from -20°C to $+60^{\circ}\text{C}$ with an accuracy of $\pm 1^{\circ}\text{C}$, while maintaining a battery life of over 3 years. In addition, the capability of the sensor-readout circuit interconnect was examined to withstand a bending radius of 0.8 mm and 30 opening and closing cycles of the container lid. Additionally, the PFS and CFS test coupons were tested and compared for performance and reliability under varying environmental and mechanical effects based on IPC-TM-650 and ASTM standards.

EXPERIMENTAL

A. Design and Fabrication

The CFS and PFS circuits were designed with Altium® Designer software (a registered trademark of Altium Limited, San Diego, California, USA). The overall dimensions of the CFS and PFS prototypes are shown in Fig. 1(a). The main components of the CFS and PFS include microcontroller unit (MCU), temperature and humidity sensor, quartz crystal, voltage regulator, joint test action group (JTAG) port, microSD™ (a trademark of SD-3C, LLC, Redmond, Washington, USA) card port, battery, and battery header connector (Fig. 1(b)). The microSD™ card was positioned at the bottom of the substrate and stiffeners were used to handle any associated stress. The JTAG port is on the top left and can be removed after programming to reduce the overall height. The HDC2022 sensor from Texas Instruments (Dallas, Texas, USA) offers high-accuracy temperature and relative humidity (RH) measurement, with ratings of $\pm 0.2^{\circ}\text{C}$ and $\pm 2\%$ RH, respectively. Additionally, the sensor is IP67-rated [23] for water and dust protection and features low power consumption. The sensor was positioned at the end of an interconnect, separated from the

circuit. This allows the sensor to be placed inside a sealed container while keeping other components outside, making data collection easier and without affecting the container's internal environment. The quartz crystal ECS-33B is placed next to the MCU in the middle of the circuit, to provide the clock signal. A 32-pin VQFN microcontroller unit (CC2640R2FRSMT) from Texas Instruments reads sensor responses, monitors battery levels, and activates visual indicators. In addition, it writes data to the microSD™ card, and uses real-time clock to sleep/wake up. Low-dropout voltage regulator (TPS70612DBVT from Texas Instruments) controls the microSD™ card voltage to minimize any potential data loss. A flexible and thin lithium battery (CP142828, $1.4 \times 29 \times 29$ mm) with 150 mAh capacity from GMBPOW® (a registered trademark of Guangzhou Markyn Battery Co., Ltd., China) was used to power the CFS and PFS. A Molex Pico-Ezmate crimp/header connector (Lisle, Illinois, USA) was used for battery connection due to its reliability and ease of use. The key materials employed in the fabrication of CFS and PFS prototype are summarized in Table S1 (Supporting Information).

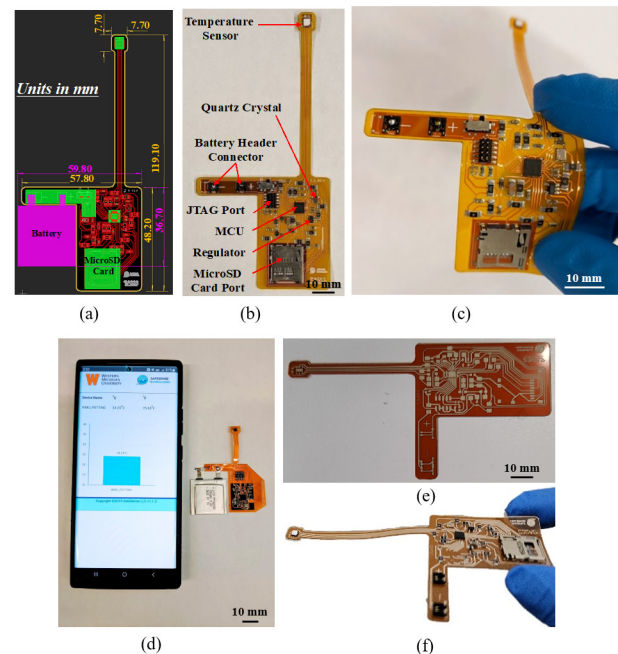


Figure 1: (a) CFS and PFS layout dimensions, (b) fabricated CFS prototype with soldered component, (c) flexible CFS prototype, (d) wireless CFS with Android™ app, (e) printed PFS, and (f) fabricated PFS prototype.

The CFS prototype PCBs were fabricated by depositing copper traces with a thickness of $35 \mu\text{m}$ onto a $88.9 \mu\text{m}$ thick polyimide flex substrate. These copper traces were deposited through the wet etching method. The polyimide substrate was then covered with a yellow overlay solder mask with a thickness of $12.5 \mu\text{m}$. The surface finish used was Electroless Nickel/Immersion Gold (ENIG). The photograph of the flexible CFS prototype is shown in Fig. 1(c). The maximum thickness of the CFS at the microSD™ card port location

was approximately 1.95 mm. Figure 1(d) shows the CFS prototype equipped with a thin-film battery and connected wirelessly via Bluetooth® (a registered trademark of Bluetooth Special Interest Group, Kirkland, Washington, USA) to an Android™ (a trademark of Google LLC, Mountain View, California, USA) application interface. However, this prototype remained unused as it did not comply with DoD requirements, which mandated data recording solely on a microSD™ card.

For the fabrication of the PFS, a stainless-steel screen with a mesh count of 325 threads per inch (TPI), emulsion thickness (MS-22) of 15 μm , ultra-thin wire diameter of 22.8 μm , and deflection angle of 22.5° was obtained from Microscreen LLC (South Bend, Indiana, USA). Conductive silver ink (DuPont™ 5025) from DuPont™ (a trademark of DuPont de Nemours, Inc. Wilmington, Delaware, USA) was then deposited on a Kapton® 500 HN substrate (Kapton® is a registered trademark of DuPont de Nemours, Inc., Wilmington, Delaware, USA). This was accomplished using an HMI MSP 485 screen printer (Lebanon, New Jersey, USA) with an offset height of 1 mm. Following this, the printed samples were cured in an Accutemp 09S vacuum oven from Across International (Livingston, New Jersey, USA) at 120 °C for 8 minutes to evaporate the solvent. The photographs of the PFS prototype are shown in Fig. 1(e) and (f). It is clearly visible that the conductive traces have been successfully deposited without any overlap. The printed PFS prototypes were then accurately cut out using a Graphtec FC8600 plotter (Yokohama, Kanagawa, Japan) as shown in Fig. S1. Following this, solder paste (Chip Quik® Solder Sn42/Bi57.6/Ag0.4) was applied to the PFS and components were attached prior to heating in the advanced Puhui T-937 reflow oven (from Taian Puhui Electric Technology Co., Ltd, Taian, Shandong, China) as shown in Fig. S2.

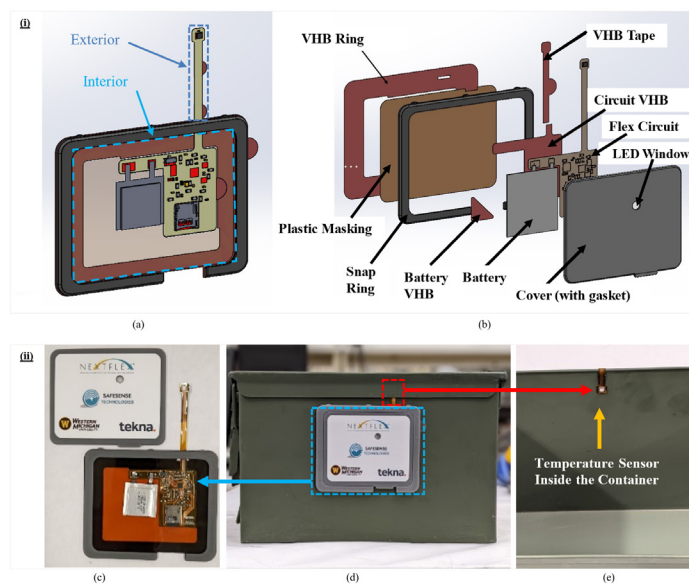


Figure 2: Snap-in enclosure: (i) illustration: (a) schematic, and (b) exploded view; (ii) fabricated prototype: (c) fabricated CFS with designed enclosure, (d) installation of enclosure on the container, and (e) installation the sensor inside the container.

The soldering challenges encountered with PFS components are detailed and illustrated in the supporting information and Fig. S3. In addition, CTFC-12 Konform® Flexcoat Conformal Coating from Chemtronics® (a registered trademark of Chemtronics, Kennesaw, Georgia, USA) and polyimide tape from Bertech® (a registered trademark of Bertech Corporation, Torrance, California, USA) company were used as a coating layer on the PFS samples.

The enclosure was designed based on several critical specifications, including the overall thickness of the device, the capacity to resist water ingress in accordance with the IP64 specification [24]. In addition, the design provides access to a microSD™ card through an open/close tab while being protected from water ingress. Figures 2(i) and 2(ii) illustrate the snap-in enclosure design and fabricated prototype, respectively. The top cover snaps into place inside the outer ring when pressed down, and can be easily removed by lifting an included tab. The enclosure was attached to the container using a double-sided 3M® VHB 5907 adhesive tape (3M® is a registered trademark of 3M Company headquartered in St. Paul, Minnesota, USA). As depicted in Fig. 2(i)(a) and (b), the flex circuits (PFS or CFS) were attached to a plastic mask (Kapton® 500 HN substrate) and enclosed inside the snap ring of the enclosure using 3M® VHB 5907 adhesive tape. A top cover was 3D printed using an acrylonitrile butadiene styrene (ABS) filament and features a foam gasket (ethylene propylene diene monomer (EPDM) closed-cell foam) which seals against water ingress when compressed. Acrylonitrile butadiene styrene provides a good balance of strength, flexibility, and necessary resistance to water, humidity, salt spray, and withstands -20°C to 60°C temperatures. A polycarbonate transparent plastic was 3D printed on the top cover to facilitate visual access to the LED indicators. Finally, a die-cut thin plastic sheet provides masking around the edge to give the foam gasket a non-adhesive surface to seal. The system was designed to meet the requirements for performance in the temperature range of -20 °C to 60 °C and have these dimensions: The interior portion (electronic readout module and battery) has a thickness of < 3.175 mm and an area of < 645.16 mm². The exterior portion (sensor and interconnect) has a thickness of < 3.175 mm and an area of < 2580.64 mm². Table S2, summarizes the materials employed in the fabrication of the enclosure prototype, and Table S3 outlines potential materials for utilization in large-scale production.

To meet the IPC-TM-650 standards for environmental and mechanical characterizations, three test coupons (“dogbone” [Fig. 3(i)(a)], “comb pattern” [Fig. 3(i)(b)], and “meander line” [Fig. 3(i)(c)] were designed using AutoCAD® software (a registered trademark of Autodesk, Inc., San Francisco, California, USA). The designs and dimensions of the test coupons are shown in Fig. 3(i), and photographs of the fabricated CFS and PFS coupons are shown in Fig. 3(ii).

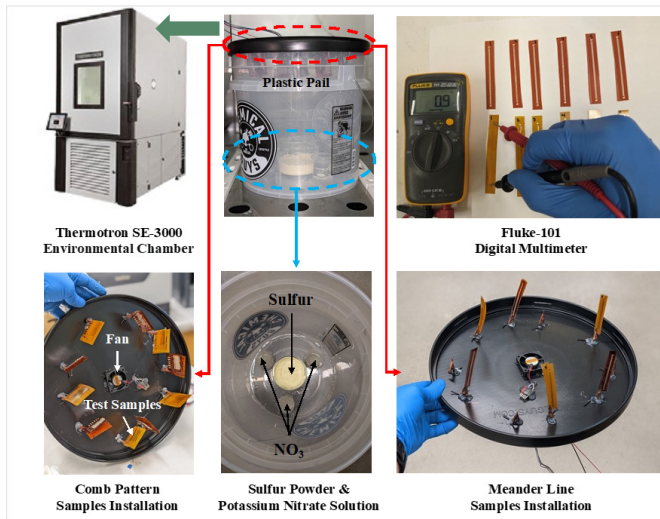


Figure 5: Experiment setup for the corrosion test.

Mechanical Tests

The mechanical testing sequence commenced with a durability test. Elongation, bending, terminal bond strength, and peel resistance were subsequently investigated as per the IPC-TM-650 2.4.18.1; IPC-TM-650, 2431-1; IPC-TM-650, 2.4.20; and ASTM D1876 standards, respectively. Mechanical tests were performed by using an Instron® 4301 tester and a Mark-10® ESM301 motorized test stand integrated with a force gauge machine (Instron® and Mark-10® are registered trademarks of Instron Corporation, based in Norwood, Massachusetts, and Mark-10 Corporation, located in Copiague, New York, respectively). A GW Instek 6100 precision LCR meter (New Taipei City, Taiwan) and a C# custom-developed software were used for recording the resistance variations.

In durability test, the effect of opening and closing the container lid on the interconnect of the CFS and PFS prototypes was examined. This investigation aimed to comprehend the durability of the copper and silver traces within the interconnect. The CFS and PFS prototypes with and without encapsulant coating was attached to the M2A2 container and connected to a GW Instek 6100 precision LCR meter (Fig. 6(a)). The CFS and PFS systems were on the front side/ exterior of the container and the interconnect was bent over the lip of the container and attached to the interior wall of the container (Fig. 6(b)). After that, the lid of the container was opened and closed 30 times and the effect of the stress/damage that occurs on the interconnect was investigated by recording the resistance across the interconnect (Fig. 6(c)).

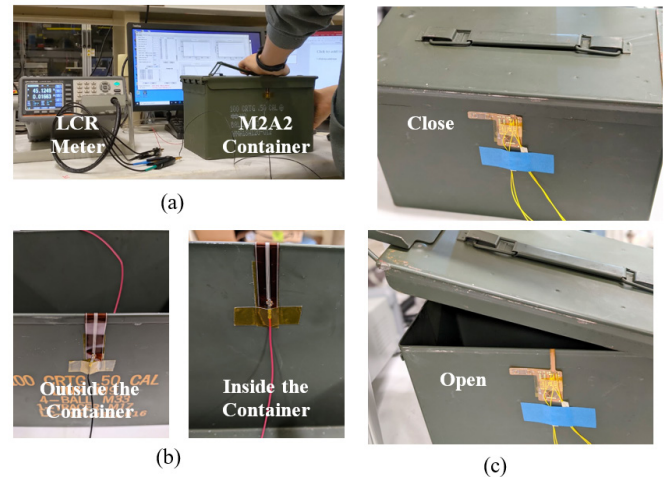


Figure 6: Durability test: (a) experiment setup, (b) inside and outside view of the container with PFS test coupon, (c) opening and closing the container lid.

Elongation test was performed using CFS and PFS “dogbone” test coupons, as per the IPC-TM-650 2.4.18.1, shown in Fig. 7(i) (a) and (b). The specimen was loaded between the clamps of an Instron® 4301 tensile tester, and the clamps were programmed to elongate the coupon at a speed rate of 0.5 mm/min [Fig. 7(i)(a)]. As the clamp elongated the test coupon, the copper or silver traces along with polyimide film were subjected to strain, which in turn created fracture leading to the tearing of the coupon [Fig. 7(i)(b)]. Elongation test was employed to extract the Young’s modulus (E), which quantifies a material’s stiffness, and is expressed as the ratio of stress (σ) to strain (ϵ). Young’s modulus can be computed using Eq. (1):

$$E = \frac{\text{Stress}}{\text{Strain}} = \frac{\sigma}{\epsilon} \text{ (Pa)} \quad (1)$$

Where, stress is the force (F) applied per unit area (A) and can be calculated using Eq. (2):

$$\sigma = \frac{F}{A} \text{ (Typically } N/m^2, \text{ or Pa)} \quad (2)$$

The area (A) is determined by multiplying the thickness and width of the specimen, measured in square meters (m^2). Stress is typically measured in Newtons per square meter (N/m^2), also known as Pascals (Pa). Strain is a measure of deformation, representing the displacement between particles in the material. Strain is calculated as the change in length (ΔL) divided by the original length (L_0) using Eq. (3):

$$\epsilon = \frac{\Delta L}{L_0} \quad (3)$$

In bending test, the “meander line” test coupon was mounted between the moving and stationary clamps of a Mark-10® test stand and the force gauge as shown in Fig. 7(ii)(c). The bonded wires of the test coupon were connected to a GW Instek 6100 precision LCR meter and a custom developed software was used for recording the resistance variations across the conductive traces during the 100-cycle bend tests [Fig. 7(ii)(d)]. The “meander line” test coupon was then subjected to a cyclic bend test, where copper and conductive printed silver traces on the specimen were bonded to wires (using crimp connectors) and subjected to a 180° bend test which is repeated for 100 cycles.

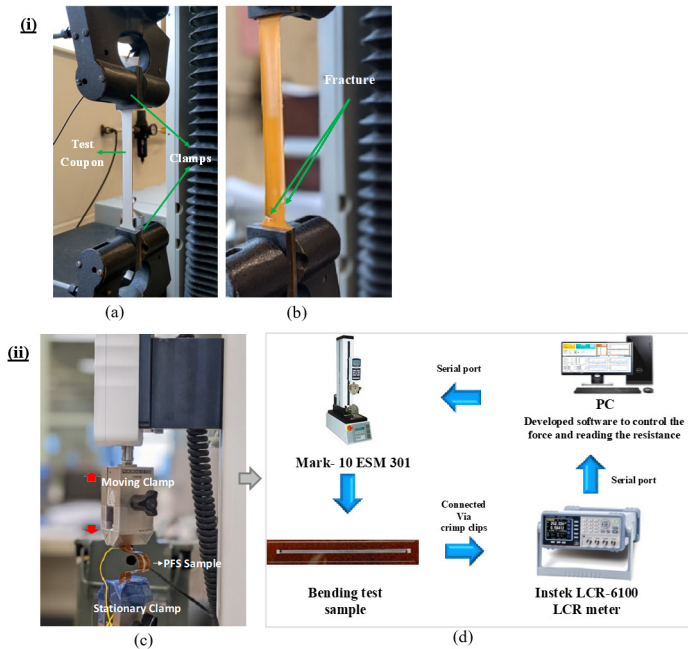


Figure 7: (i) Elongation test: (a) dogbone test coupon placed between the tensile tester clamps, and (b) fracture on test coupon; (ii) bend test: (c) meander line test coupon subjected to bending, and (d) experiment setup for bending test.

In terminal bond strength test, the terminal pad on the PCB was bonded to a wire with length of 5 cm using a traditional 60W soldering device and an Alpha Fry rosin core solder wire (tin/lead -60/40) (Elizabeth, New Jersey, USA) [Fig. 8(i)(a)]. The sample was placed on the Mark-10® test stand and the free end of the bonded wire was attached to the vertically movable clamp. The bonded wire was pulled at a rate of 50 mm/min with the movable clamp and the force required to remove/detach the wire was recorded using the force gauge of the Mark-10® test stand [Fig. 8(i)(b)].

Peel test was performed to investigate the adhesion strength of the double-sided adhesive tape used for attaching the CFS/PFS to the enclosure and subsequently to the container, as shown in Fig. 8(ii)(c) and (d). This was completed in accordance with the ASTM D1876 standard, by attaching a 127 mm long 3M® VHB 5907 adhesive tape to the ammunition container. The container was cut into small strips, enabling the uniform attachment/detachment of the adhesive to/from the container. The ammunition container

strips were held between two static clamps; while the adhesive attached to the container was held between two vertically movable clamps of the Instron® 4301 tester via a polyimide film, as shown in Fig. 8(ii)(c). The clamps holding the Kapton® film attached to the adhesive were programmed to move vertically at a rate of 254 mm/min and the corresponding forces required to peel off the adhesive were recorded by the tester. A similar test was repeated by replacing the polyimide film with the ABS pieces (Note: ABS was used to make the enclosure) [Fig. 8(ii)(d)].

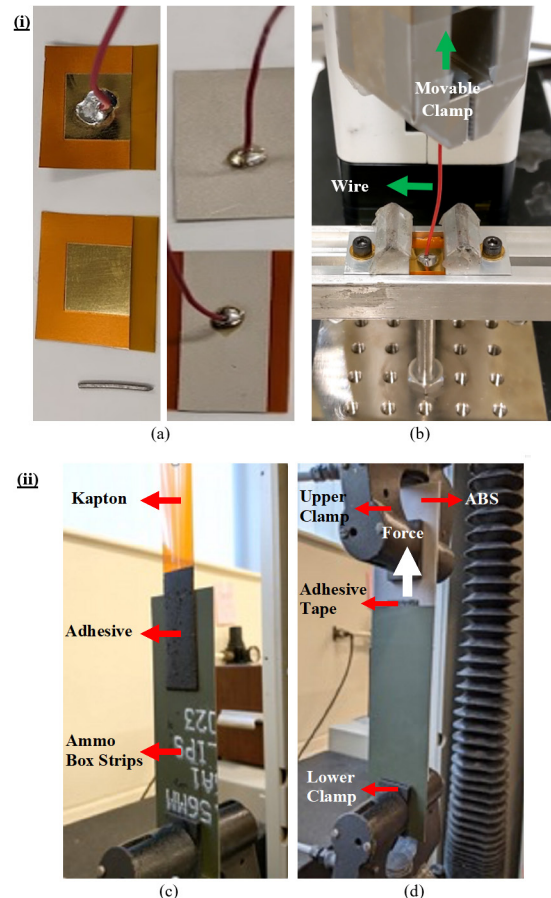


Figure 8: (i) Terminal bond strength test: (a) soldering on terminal pad, and (b) soldered wire attached to the movable clamp; (ii) peel test: ammunition container strips with adhesive and (c) Kapton®, and (d) ABS placed between the Instron® 4301 tester clamps and peeling off the adhesive from the container.

RESULTS AND DISCUSSION

Surface Morphology

In this characterization, a thickness of $10.50 \pm 0.10 \mu\text{m}$ and roughness of $1.48 \pm 0.03 \mu\text{m}$ was measured for the printed samples, as shown in Fig. 9(a) and (b), respectively. From the SEM image shown in Fig. 9(c), it is evident that the silver film is homogeneously printed, and the silver flakes are uniformly spread without any cracks. The cross-sectional view of the printed film with encapsulant clearly shows the uniform deposition of encapsulant (with thickness of $48.60 \pm 0.30 \mu\text{m}$) on the printed film (Fig. 9(d)).

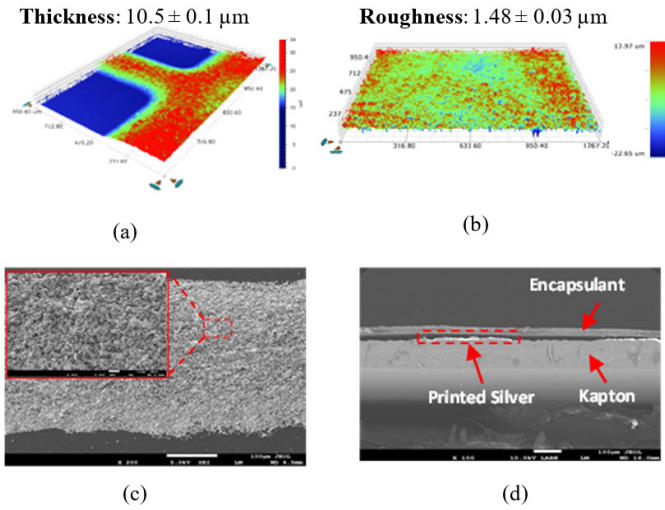


Figure 9: Surface morphological characterization of PFS: (a) thickness, and (b) roughness, (c) high magnification SEM image of printed silver and (d) cross-sectional SEM image of encapsulant on printed traces of Kapton®.

Environmental Tests

During the functional test to evaluate the performance of the sensor, the temperature of the chamber was continuously increased stepwise from -20 °C to 60 °C (in steps of 2 °C and step time of 15 minutes) and responses of the thermometer and the sensor response were recorded. As shown in Fig. 10, the sensor response was matched with the thermometer and is linear from -20 °C to 60 °C, with a correlation factor of almost unity. This calibration graphs and its equations were used in the programming code of the MCU to calibrate the response read by the temperature sensor for different humidity ranges to increase the accuracy.

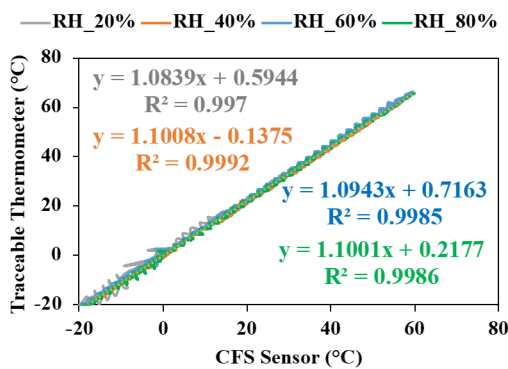


Figure 10: Calibration curve and equations in different RH%.

The effect of humidity on the sensor performance was investigated by varying RH levels from 20% RH to 80% RH, in steps of 20%. Initially, at 20% RH step, the temperature of the chamber was increased from -20 °C to 60 °C, and then decreased to -20 °C, in steps of 2 °C, with a step time of 15 minutes (Fig. S4). The responses of the temperature and humidity sensor (ST),

thermometer (TT) and chamber (CT) were recorded. This same temperature sweep was repeated at different relative humidity levels (40% RH, 60% RH, and 80% RH), and the temperature and humidity responses were recorded. It was observed that temperature and humidity sensor clearly follow the temperature and humidity variations in the chamber.

In moisture and insulation resistance test, the resistance of the PFS and CFS samples with and without encapsulant coating was measured every 24 hours and was found to be stable at $\approx 18 \text{ M}\Omega$ for coated CFS (Fig. 11(a)), coated and uncoated PFS test coupons (Fig. 11(b)) which is also reported in our previous work [21]. On the other hand, CFS test coupons without solder mask experienced resistance shift (Fig. 11(a)) and permanent change in color that can be attributed to the oxidation of copper [Fig. 11(c) and (d)]. This clearly shows that coating layer plays a significant role to protect the copper from oxidation while printed silver layer has not been affected by the moisture and temperature variations.

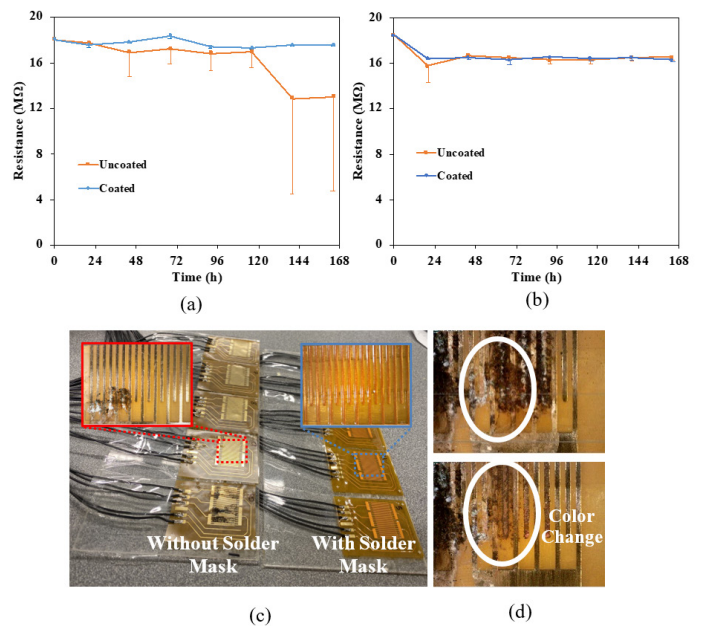


Figure 11: Moisture and insulation resistance test: (a) CFS resistance response, (b) PFS resistance response, (c) CFS comb pattern test coupons with and without solder mask, and (d) color change of CFS after IPA cleaning.

After the completion of the corrosion test, the “meander line” test coupons’ weight change was measured as $0.35 \pm 0.03\%$ after 72 hours for both coated CFS and uncoated CFS samples (Fig. 12(a)). Similarly, the PFS samples covered with a polyimide tape (from Bertech® company) exhibited a maximum weight change of $0.33 \pm 0.02\%$ whereas PFS samples uncoated and coated with Chemtronics® CTFC-12 exhibited a weight change of $0.95 + 0.27\%$ (Fig. 12(b)). The maximum relative resistance changes of “meander line” test coupons’ was measured as $\approx 0\%$ for coated CFS, uncoated CFS, and coated PFS with a polyimide tape, while it was measured as $367.75 \pm 32.35\%$ for uncoated PFS. The maximum relative weight change of the CFS “comb pattern” test coupons’

after 144 hours was measured as $0.26 \pm 0.03\%$ and $0.34 \pm 0.07\%$ for coated and uncoated samples, respectively. Similarly, the weight change was measured as $0.37 \pm 0.10\%$ and $0.83 \pm 0.04\%$ for the samples coated with Chemtronics® CTFC-12 and uncoated PFS “comb pattern” test coupons, respectively. This clearly indicates that the CFS samples (both coated and uncoated) and coated PFS samples were not affected by sulfur vapors or high humidity and temperature, and resisted against corrosion unlike uncoated PFS samples. The microscopic images of the CFS and PFS samples are shown in Fig. S5. No visible corrosion was observed on the copper traces of both coated and uncoated samples (Fig. S5(a) and (b)). Although the uncoated PFS samples exhibited corrosion (as depicted in Fig. S5(c)), those coated with polyimide remained unaffected by corrosion [illustrated in Figure S5(d) and (e)]. In addition, pictures show that polyimide has provided a better protection against corrosion when compared to Chemtronics® CTFC-12 spray coat (Fig. S5(e)).

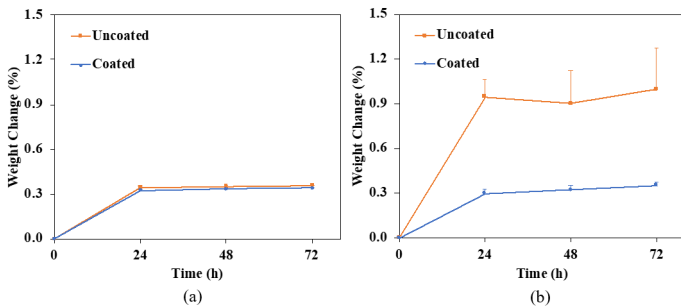


Figure 12: Corrosion test, meander line test coupons' weight change: (a) CFS, and (b) PFS.

Mechanical Tests

In durability test, the lid of the container was opened and closed 30 times (Fig. 13(a)) resulted in an average resistance change of $0.16 \pm 0.08\%$ and $0.13 \pm 0.05\%$ for the coated and uncoated CFS samples (Fig. 13(b)). This clearly shows a very minimal impact on the interconnect lines of CFS.

Similarly, a PFS resistance change of $3 \pm 0.35\%$ and $24 \pm 1.85\%$ was measured for the prototypes that were coated with Chemtronics® CTFC-12, as well as for the uncoated samples, respectively, when opening and closing the lid after 30 cycles (Fig. 13(c)). The average resistance change clearly shows that there is very minimal impact of the container lid on the interconnect lines coated with encapsulant when compared to uncoated samples. Similar results were observed when examining the coated and uncoated samples using microscopic and SEM images. As shown in Fig. S6(a) and (b), the microscopic images of coated sample clearly show that there was no visible damage to the silver traces under the encapsulant and silver nanoflakes were strongly attached to the polyimide substrate even after the test. However, the microscopic and SEM images of the uncoated samples clearly indicate the damage sustained by the printed traces and detachment of silver nanoflakes from the polyimide substrate [Fig. S6(c) and (d)]. High magnification images (Fig. S6(d)) revealed the impressions of the container on the silver nanoflakes of the areas where the silver particles were partially detached.

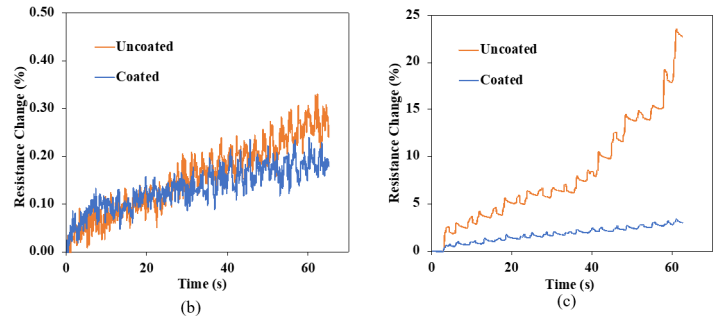
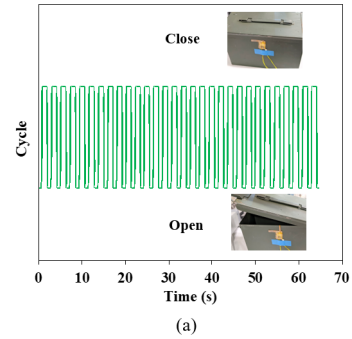


Figure 13: (a) 30 cycles opening and closing the container lid, resistance changes of the (b) CFS, and (c) PFS while opening and closing the container lid.

In elongation test, the stress versus strain graphs for CFS and elongated samples with encapsulant coating layer are shown in [Fig. 14(a) and (b)]. In each test, the test coupon was elongated until it breaks, and the force required to break/tear the test coupon was recorded. An average stress of 121.10 ± 1.20 MPa and 83.40 ± 2.30 MPa was measured to break/tear the CFS and PFS test coupons respectively. Furthermore, a Young's modulus of 7.17 GPa and 2.6 GPa was calculated from linear the region of the stress-strain characteristic curves of CFS and PFS test coupons, respectively. In addition, the results of PFS samples with and without Chemtronics® CTFC-12 did not exhibit a meaningful difference between the stress-strain curves of the coated and uncoated layers.

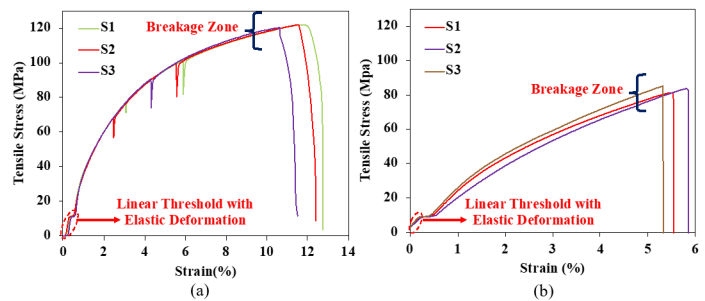


Figure 14: Elongation test: stress-strain curves of (a) CFS, and (b) PFS.

In bending test, during each cycle, both CFS and PFS samples demonstrated minimal average resistance changes, with CFS showing a change of approximately 0% when transitioning from an idle to a bend status, and PFS registering a slight 0.1% change under similar conditions. Furthermore, after subjecting the systems to 100 cycles, equivalent to 28 minutes for both CFS and PFS, the resistance response exhibited different behaviors. As shown in Fig. 15(i)(a), CFS maintained a nearly stable response, exhibiting an approximate 2.3% drift between the initial and final cycles. In contrast, PFS sample showed a noticeable increase in resistance, measuring an approximately 6% drift over the same period [Fig. 15(i)(b)]. In addition, SEM micrographs of the printed sample before and after bend test were obtained and are shown in Fig. 15(ii)(c) and (d), respectively.

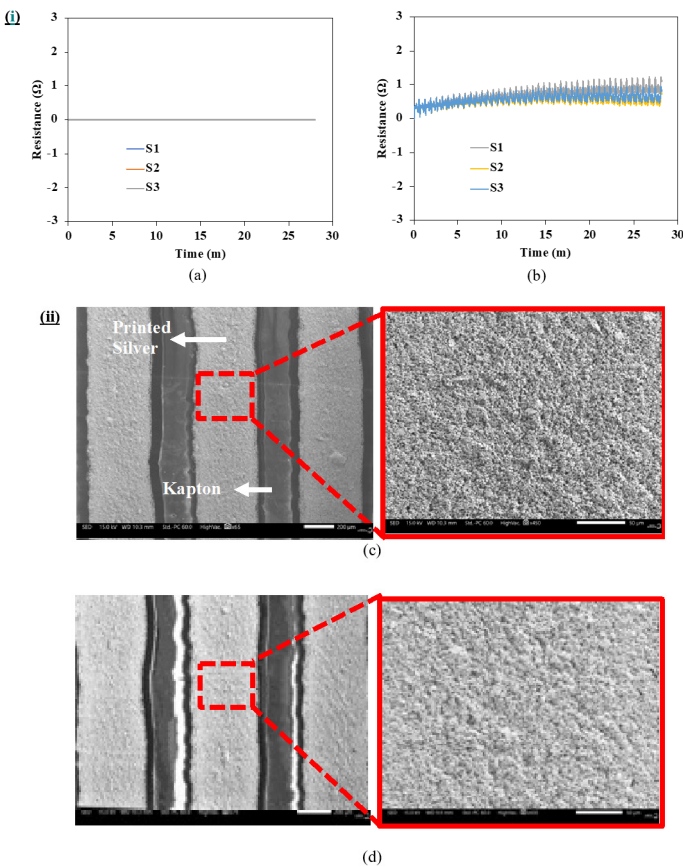


Figure 15: Bend test: (i) resistance response of the test coupon subjected to 180° bend: (a) CFS, and (b) PFS; (ii) SEM micrographs of printed test coupon (c) before bending, and (d) subjected to 180° bend.

In terminal bond strength test, the soldered wire broke/detached from the terminal pad when an average force of 43 N and 3.8 N was applied to CFS and PFS samples, respectively [Fig. 16(i)(a) and (b)].

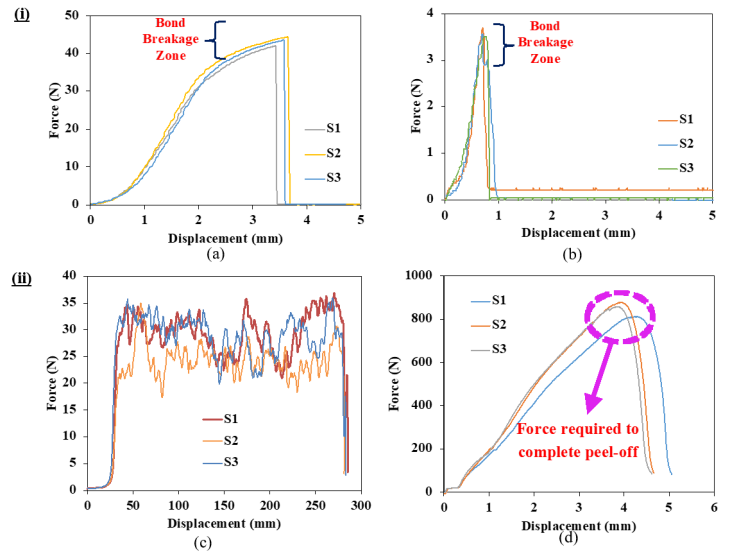


Figure 16: Terminal bond strength test: (i) force required to peel off the wire from (a) CFS, and (b) PFS; (ii) peel test: force required to peel off (c) Kapton®, and (d) ABS from ammunition container stripes with adhesive.

In peel test, shown in Fig. 16(ii)(c), an average force of 25 N was required to completely remove the adhesive and polyimide from the container. This force corresponds to the peeling-off of the temperature sensor on the polyimide interconnect attached to the inside of the ammunition container. Figure 16(ii)(d) shows the direction and average of force (750 N) that was required to completely remove the ABS with adhesive from the ammunition container and this force corresponds to peeling off the enclosure attached to the outside of the container.

The environmental and mechanical characterizations as well as reliability tests on both the CFS and PFS were performed based on IPC-TM-650 and ASTM test standards and is summarized in Table 1.

Table 1: Comparison summary of CFS and PFS.

Test	Standard	Measured Parameter	Test Coupons Pattern	CFS		PFS	
				Coated	Uncoated	Coated	Uncoated
Durability	-	Resistance Change (%)	Prototype	0.008	0.011	3	24
Moisture & Insulation Resistance	IPC-TM-650, 2.6.3-H	Resistance Change (%)	Comb	0	60	0	0
Corrosion	ASTM E-595	Weight Gain (%)	Comb & Meander Line	<0.4	<0.4	<0.4	<1.3
		Resistance Change (%)	Meander Line	≈0	≈0	≈0	<400
Elongation	IPC-TM-650, 2.4.18.1	Young's Modulus (Gpa)	Dogbone	717	717	2.6	2.6
Bending	IPC-TM-650, 2.4.3-1	Resistance Change (%)	Meander Line	0	0	0.1	0.1
Terminal Bond Strength	IPC-TM-650, 2.4.20	Force (N)	Rectangle (30 × 15 mm)	-	43	-	3.6

CONCLUSION

This paper introduces a novel FHE-based solution for continuous monitoring of temperature inside a sealed storage container. Mechanical characterizations, including the durability and terminal bond strength tests were conducted, revealing that the CFS version exhibits superior reliability compared to the PFS. In addition, the elongation tests show a lower Young's Modulus of PFS which is desirable to obtain higher flexibility when compared to the CFS version. Both CFS and PFS with encapsulation layer performed similarly in the moisture and insulation resistance test, bending, corrosion, and peel tests. This clearly shows that PFS can perform similar to the CFS if the terminal bond strength (which depends on the solder paste adhesion with the silver ink on the terminal pad) can be improved by identifying the appropriate solder paste. Overall, the PFS system provides a cost-effective solution, with a total cost of under \$20, for monitoring temperature within a DoD-relevant ammunition container. Future work will concentrate on characterizing the humidity sensing capability of the developed CFS and PFS across relative humidity changes, ranging from 10% RH to 90% RH.

AUTHOR CONTRIBUTION

M. Panahi and A. J. Hanson contributed equally. The manuscript was written through contributions of all authors. All authors have given approval to the final version of the manuscript.

ACKNOWLEDGMENT

This material is based on research partially sponsored by Air Force Research Laboratory and NextFlex under Agreement Number FA8650-20-2-5506. The U.S. Government is authorized to reproduce and distribute reprints for Governmental Purposes notwithstanding any copyright notation thereon.

The authors identify several commercial products, the mention of which is necessary for the completeness of this manuscript. However, these mentions should not be construed as an endorsement of those products. In addition, the authors would like to thank Rob Feeman, and Wade Rutkoskie from Tekna Inc. for supporting the enclosure design and fabrication.

REFERENCES

- [1] M. Marzencki et al., "Remote health, activity, and asset monitoring with wireless sensor networks," 2011 IEEE 13th International Conference on e-Health Networking, Applications and Services, 2011, pp. 98-101, doi: 10.1109/HEALTH.2011.6026796.
- [2] P. M. Hart, "Continuous asset monitoring on the smart grid," 2011 IEEE PES Innovative Smart Grid Technologies, 2011, pp. 1-7, doi: 10.1109/ISGT-Asia.2011.6167132.
- [3] H. Niu and S. Jagannathan, "High memory passive RFID tags with multimodal sensor design and application to asset monitoring in-transit," 2013 IEEE International Instrumentation and Measurement Technology Conference (I2MTC), 2013, pp. 1615-1619, doi: 10.1109/I2MTC.2013.6555687.
- [4] S. Kulkarni, K. Ashok, F. Lambert and D. Divan, "Asset monitoring using smart sensing and advanced analytics for the distribution network," 2019 North American Power Symposium (NAPS), 2019, pp. 1-6, doi: 10.1109/NAPS46351.2019.9000254.
- [5] M. Panahi, S. Masihi, A. Hanson, J. R. Rodriguez-Labra, A. Masihi, D. Maddipatla, B. B Narakathu, D. Lawson, M. Z. Atashbar, "Development of a flexible smart wearable oximeter insole for monitoring SpO2 Levels of diabetics' foot ulcer," in IEEE Journal on Flexible Electronics, doi: 10.1109/JFLEX.2022.3232465.
- [6] Y. Lu et al., "Multimodal plant healthcare flexible sensor system," ACS Nano 2020 14 (9), 10966-10975, doi: 10.1021/acsnano.0c03757.
- [7] US Food and Drug Administration, Available: <https://www.fda.gov/news-events/press-announcements/fda-brief-fda-authorizes-longer-time-refrigerator-storage-thawed-pfizer-biontech-covid-19-vaccine>, [Accessed Dec. 1, 2023].
- [8] P. Escobedo, M. Bhattacharjee, F. Nikbakhtnasrabadi and R. Dahiya, "Flexible strain and temperature sensing nfc tag for smart food packaging applications," in IEEE Sensors Journal, vol. 21, no. 23, pp. 26406-26414, 1 Dec.1, 2021, doi: 10.1109/JSEN.2021.3100876.
- [9] PC 5.8: Temperature and Humidity Monitoring Tag, Available: <https://www.nextflex.us/project-call/project-call-5-0/>, [Accessed Dec. 1, 2023].

[10] S. Nakata, T. Arie, S. Akita, K. Takei, “wearable, flexible, and multifunctional healthcare device with an ISFET chemical sensor for simultaneous sweat pH and skin temperature monitoring,” *ACS Sensors* 2017 2 (3), 443-448, doi: 10.1021/acssensors.7b00047.

[11] S. Masihi et al., “Development of a flexible tunable and compact microstrip antenna via laser assisted patterning of copper film,” in *IEEE Sensors Journal*, vol. 20, no. 14, pp. 7579-7587, 15 July 2020, doi: 10.1109/JSEN.2020.2987318.

[12] S. Masihi et al., “Development of a flexible wireless ECG monitoring device with dry fabric electrodes for wearable applications,” *IEEE Sensor Journal*, doi:10.1109/JSEN.2021.3116215, 2021.

[13] S. Hajian et al., “Humidity sensing properties of halogenated graphene: a comparison of fluorinated graphene and chlorinated graphene,” 2020 IEEE International Conference on Flexible and Printable Sensors and Systems (FLEPS), Manchester, UK, 2020, pp. 1-4, doi: 10.1109/FLEPS49123.2020.9239564.

[14] X. Zhang et al., “Printed carbon nanotubes-based flexible resistive humidity sensor”, *IEEE Sensors Journal*, vol. 20(21), pp. 12592-12601, 2020, doi: 10.1109/JSEN.2020.3002951.

[15] A. K. Bose et al., “Highly sensitive screen printed strain gauge for micro-strain detection,” 2019 IEEE International Conference on Flexible and Printable Sensors and Systems (FLEPS), Glasgow, UK, 2019, pp. 1-3, doi: 10.1109/FLEPS.2019.8792282.

[16] M. Panahi et al., “A smart wearable oximeter insole for monitoring SpO₂ levels of diabetics’ foot ulcer,” 2022 IEEE International Conference on Flexible and Printable Sensors and Systems (FLEPS), Vienna, Austria, 2022, pp. 1-4, doi: 10.1109/FLEPS53764.2022.9781511.

[17] S. Masihi, et al., “A highly sensitive porous PDMS-based capacitive pressure sensors fabricated on fabric platform for wearable applications,” *ACS Sens.*, 6, pp. 938-949, 2021, doi: 10.1021/acssensors.0c02122.

[18] S. G. R. Avuthu, B. B. Narakathu, M. Z. Atashbar, M. Rebros, E. Hrehorova, B. Bazuin, P. D. Fleming, M. K. Joyce, “Printed capacitive based humidity sensors on flexible substrates,” *Sensor Letters*, Vol. 9, 1-3, 2011. doi: 10.1166/sl.2011.1633.

[19] S. Hajian et al., “Flexible Capacitive Humidity Sensor Based on Fluorinated Graphene,” *IEEE Sensors Conference*, pp. 1-4, 2019. doi: 10.1109/SENSOR43011.2019.8956564.

[20] M. Panahi et al., “Investigation of temperature effect on the porosity of a fabric based porous capacitive pressure sensor,” *IEEE International Conference on Flexible and Printable Sensors and Systems (FLEPS)*, pp. 1-4, 2020, doi: 10.1109/FLEPS49123.2020.9239439.

[21] M. Panahi et al., “Development of a FHE based temperature and humidity sensing system for asset monitoring applications,” 2022 IEEE Sensors, Dallas, TX, USA, 2022, pp. 01-04, doi: 10.1109/SENSOR52175.2022.9967273.

[22] M. Panahi et al., “Flexible hybrid electronics based condition monitoring system for sealed containers,” 2023 IEEE International Conference on Flexible and Printable Sensors and Systems (FLEPS), Boston, MA, USA, 2023, pp. 1-4, doi: 10.1109/FLEPS57599.2023.10220372.

[23] International Electrotechnical Commission, “Degrees of protection provided by enclosures (IP Code) - IP67: Dust tight and protected against the effects of temporary immersion in water,” in IEC Standard 60529, ed: IEC, 2013.

[24] International Electrotechnical Commission, “Degrees of protection provided by enclosures (IP Code) - IP64: Dust tight and protected against splashing water,” in IEC Standard 60529, ed: IEC, 2013.

BIOGRAPHIES



Masoud Panahi is a Research Assistant at the Center for Advanced Smart Sensors and Structures (CASSS), pursuing his Ph.D. degree in Electrical Engineering at Western Michigan University (WMU), Kalamazoo, MI, USA; where he also completed his M.S. degree in 2021. He has also worked as a Teaching Assistant for several semesters at the Department of Electrical and Computer Engineering, WMU. His research interests include machine learning, embedded systems, wearables and biomedical sensors, flexible hybrid electronics, and physiological signal processing. In 2022, he received the All University Graduate Research and Creative Scholar Award from WMU, which can be highlighted among many other awards he received during his M.S. and Ph.D. degree.



Anthony J. Hanson was born in Lowell, Michigan in 1995. He received his B.S. and M.S. in electrical engineering and currently working on his Ph.D. from Western Michigan University, Kalamazoo, MI. While getting his degree, he was involved with the IEEE student branch. Starting in 2017, he joined as a Research Assistant for the Center for Advance Smart Sensors and Structures (CASSS) at Western Michigan University, Kalamazoo, MI. His research interest includes sensor applications, e-textiles, flexible hybrid electronics, embedded systems, and sensor acquisition methods. Mr. Hanson awards and honors include 2019 Department-Level Graduate Research and Creative Scholars Award, Research Excellence Award, 2023 All-University Graduate Student Teaching Effectiveness Award and graduating from the Lee Honors College.



Dr. Dinesh Maddipatla received his B.E. degree in Electrical and Electronics Engineering from Anna University, India in 2013; the M.Sc. degree in Electrical Engineering from Western Michigan University, USA in 2016 and Ph.D. in Electrical and Computer Engineering (ECE) from Western Michigan University (WMU), USA in 2020. From 2020 to 2023, he was a Postdoctoral Fellow and then worked as a Research Associate with the Center for Advanced Smart Sensors and Structures (CASSS), WMU, USA. He also worked as an Electrical Engineer at Safesense Technologies, LLC, USA from 2020 to 2022. He is currently working as an Assistant

Professor at the ECE department, WMU, USA. He was awarded the Technology Transfer Talent Network (T3N) from the State of Michigan, the All-University Research and Creative Scholar Award, and the Dissertation Completion Fellowship from Western Michigan University. His research interests include all aspects of design, fabrication, and characterization of printed electronics focusing on flexible sensor structures, physical and chemical sensors, gas sensors, energy storage devices (batteries), and lab-on-a-chip sensing systems. He is a reviewer for more than 35 international journals, associated editor for 3 journals, and has published over 130 refereed journal articles and refereed conference proceedings. In addition, he has over 15 patents and invention disclosures. He is a Technical Working Group member for NextFlex, a DoD Funded Consortium for Flexible Hybrid Electronics.



Simin Masihi received her Ph.D. degree from Western Michigan University (WMU), Kalamazoo, MI, USA, in 2022. She is currently a tenure track Assistant Professor with the Department of Electrical and Computer Engineering, WMU. Her research is primarily focused on wearables and health monitoring applications and involves

the design and development of electronic devices based on emerging field of flexible hybrid electronics (FHE). These devices can seamlessly integrate into the Internet, and the addition of machine learning capabilities will enable patient monitoring in a less supervised setting. She has a great passion in having a positive influence on people's health and quality of life by making healthcare services more accessible to people all around the world. She works on development of various biosignal acquisition systems such as electrocardiogram (ECG), Pulse Photoplethysmography (PPG), and electroencephalogram (EEG). She also works on haptic systems and robotic-assisted medical systems for rehabilitation applications. Her research has resulted in over 40 peer reviewed prestigious journal publications, international proceedings, intellectual property disclosures, and patent applications, and has been featured in various news media such as The Academic Times, AZoSensors, and the SCIENMAG Science Magazine. Masihi is a member of the Institute of Electrical and Electronics Engineers (IEEE) and the American Heart Association (AHA).



Dr. Binu B. Narakathu received the B.E. degree in Electronics and Communication Engineering from Visvesvaraya Technological University, Bengaluru, India; the M.Sc. degree in Computer Engineering from Western Michigan University, USA, in 2009; and the Ph.D. degree from the Department of Electrical and Computer Engineering, at Western Michigan University, USA in 2014. From 2015 to 2017, he was a Post-Doctoral Research Fellow with the Sensor Technology Laboratory (STL), Department of Electrical and Computer Engineering, Western Michigan University, USA. From 2017 to 2019, Dr. Narakathu was a Research Associate in the Center for Advanced Smart Sensors and Structures (CASSS),

Department of Electrical and Computer Engineering, Western Michigan University, USA. He is currently an Adjunct Professor in the Department of Electrical and Computer Engineering, Western Michigan University, USA. Dr. Narakathu is also the Co-Founder and President of SafeSense Technologies, a company providing innovative sensor technology solutions for the consumer and defense markets. He has authored over 160 peer-reviewed journal and conference publications. Dr. Narakathu has been granted 7 patents and published more than 30 invention disclosures. His research interests include all aspects of design, fabrication and characterization of flexible hybrid electronics (FHE) based sensors and sensing systems integrating microfluidics, lab-on-chip systems, bio-chemical sensors, bio-electronics, and bio-MEMS devices.



Dr. Bradley J. Bazuin is currently the Chair and a Professor of Electrical and Computer Engineering with Western Michigan University, Kalamazoo, MI, USA. His current research interests include printed electronics, hybrid flexible electronic, wearable medical electronics systems, embedded signal processing, and advanced digital signal processing. He is a founding member of the WMU's Center for the Advancement of Printed Electronics (CAPE) and the Center for Smart Sensors, and Structures (CASSS). Dr. Bazuin earned his B.S. degree in Electrical Engineering from Yale University and M.S. and Ph.D. degrees in Electrical Engineering from Stanford University, Stanford, CA, USA. Before joining WMU, he was a senior systems engineer and principal engineers for nearly twenty years working on wireless communications systems in Sunnyvale, CA.



Dr. Scott Miller is the Director of Technology at NextFlex, America's Flexible Hybrid Electronics (FHE) Manufacturing Institute. Dr. Miller is responsible for the portfolio of technical projects funded by NextFlex, its Technical Council and Technical Working Groups, development of FHE industry roadmaps, initiatives within the Institute, and relationships with government, industry, and academic partners. Scott earned his Ph.D. in Chemical Engineering from Princeton University, where he did research on large area electronics manufacturing based on printing processes. Prior to joining NextFlex, Scott led industrial R&D groups in areas including printed, flexible, and hybrid electronics; wearable devices; additive manufacturing; and bioprinting and biofabrication.



Dr. Massood Z. Atashbar received the B.Sc. degree in electrical engineering from the Isfahan University of Technology, Iran, in 1989, the M.Sc. degree in electrical engineering from the Sharif University of Technology, Iran, in 1992, and the Ph.D. degree from the Department of Communication and Electronic Engineering, Royal Melbourne Institute of Technology University, Melbourne,

Australia, in 1998. From 1998 to 1999, he was a Post-Doctoral Fellow with the Center for Electronic Engineering and Acoustic Materials, Pennsylvania State University, USA. He is currently a Presidential Innovation Professor, Distinguished Faculty Scholar, a Professor of electrical and computer engineering department, and the Founding Director at the Center for Advanced Smart Sensors and Structures (CASSS), Western Michigan University, USA. He has authored or co-authored more than 350 refereed articles, refereed conference proceedings, and four book chapters. In addition, he has more than ten patents and 35 intellectual disclosures. His research interests include physical and chemical sensor development, wireless sensors, energy storage, and nanotechnology applications in sensors and flexible hybrid electronic devices. Dr. Atashbar is a Fellow of IEEE and NextFlex, a DoD Funded Consortium for Flexible Hybrid Electronics. He is currently serving as the Co-Chair of the Technical Working Group for NextFlex.

Intermetallic Compounds in Solder Alloys: Common Misconceptions

Dave Hillman¹, Tim Pearson², Richard Coyle³

¹Hillman Electronic Assembly Solutions, LLC
Cedar Rapids, IA, USA

²Collins Aerospace
Cedar Rapids, IA, USA

³Nokia
Murray Hill, NJ, USA

ABSTRACT

The Intermetallic compounds (IMC) or intermediate phases are formed between two or more metallic elements in many metal alloy systems. During soldering, an IMC is formed at the soldered interface as the molten solder reacts with an element in the substrate. IMCs also can form within the bulk solder as the joint solidifies. IMCs have critical roles in the solder joint quality and reliability. Unlike most metal alloys, an intermetallic compound typically has a fixed stoichiometry and is in variance with the conventional phases or constituents in the metal system (e.g., alpha and beta). IMCs have a different crystal structure than any of its constituents and some but never all the characteristics and properties of its constituents. Ductility is an important solder joint property, and the low intrinsic ductility of IMCs is associated with brittle behavior and reliability risk in service. However, a review of published solder field failures shows little evidence that IMC properties or IMC evolution under service conditions reduce solder joint reliability. Most IMC-induced solder joint failures are found to result from incorrect material specification or uncontrolled soldering processes. This paper describes the IMCs that occur typically in eutectic, Sn63Pb37 solder and near-eutectic SAC305 or other tin-based Pb-free solder alloys, including how they impact solder joint reliability. The paper also describes the potential impact of IMCs on the solder joint reliability for the newest generation of Pb-free high-performance solder alloys.

Key Words: Intermetallic Compound (IMC), tin/lead solder, Pb-free solder

INTRODUCTION

In soldering, an IMC is formed by the reaction of the molten solder with the substrate and is a critical element in solder joint reliability. The thickness of this metallurgical bond increases with

the time the molten solder is in contact with the substrate being soldered. Tin based solder alloys form an IMC thickness that is typically 1-3 μm for most soldering processes used in the printed circuit assembly processes [1]. The IMC thickness increases as the solder joint ages in the solder state. The physical properties of IMCs are typically quite different than the solder and substrate materials. In general IMCs are stronger and have lower ductility (aka being more brittle) which can have an effect on the overall solder joint reliability. Excessive IMC thickness due to incorrect or out of control soldering processes can become a crack initiation region during the deformation of a solder joint. Although solder alloys are regarded as ductile materials, they can exhibit brittle physical properties under certain conditions. Figure 1 illustrates how a variety of solder alloys all undergo have ductile to brittle behavior with decreasing temperature. IMC phases can also be found in the solder microstructure matrix where they can affect the solder joint microstructure and properties.

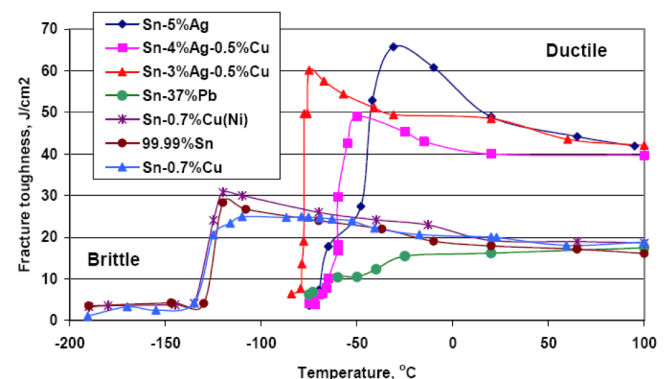


Figure 1: Solder Alloy Ductile to Brittle Behavior [2]

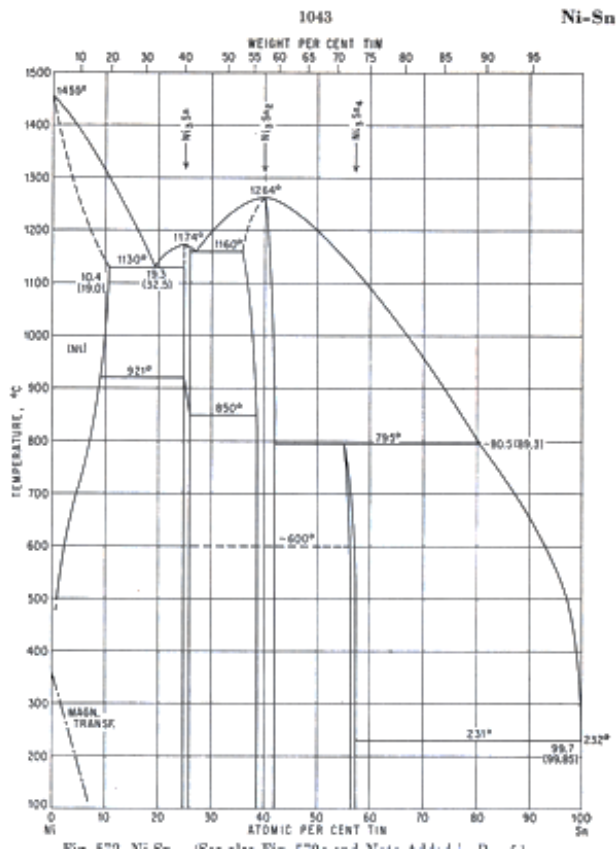


Figure 5: Tin Nickel Phase Diagram [3,4]

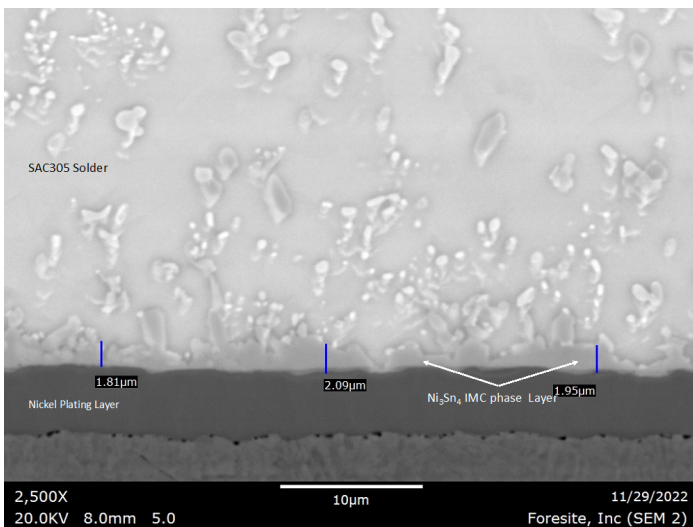


Figure 6: Ni_3Sn_4 IMC Phase at the Solder Joint/Substrate Interface (Photo courtesy of Terry Munson, Foresite)

IMC PHASES IN SAC SOLDER ALLOYS

The Sn-based SAC alloys form the same copper IMC phases (Cu_6Sn_5 , Cu_3Sn) as discussed in the SnPb solder alloy section. Hodulova et.al. [7], using thermal aging processing post soldering, determined that the Cu_6Sn_5 phase formed during the soldering

process and the Cu_3Sn phase formed during thermal aging. The Cu_3Sn phase thickness was limited by the Cu_6Sn_5 phase acting as a diffusion inhibitor. The copper IMC phases growth and thicknesses are sensitive to the higher copper concentrations found in the Sn-based SAC alloys.

In addition to the copper and nickel-based IMC phases discussed, the Sn-based, SAC alloys have silver-tin IMC phases too, since they utilize Ag as a primary constituent element addition. The tin/silver phase diagram (Figure 7) shows solubility of Ag in Sn of less than 0.1 wt. % up to 200°C (Ag_3Sn IMC indicated as ζ phase). During solidification of SAC solders, the Ag and Sn react to form networks of Ag_3Sn precipitates at the primary Sn dendrite boundaries (Figure 8).

ence of the ζ phase, first detected by potential measurements [14] and definitively established by thermal and micrographic studies [4], was confirmed by X-ray investi-

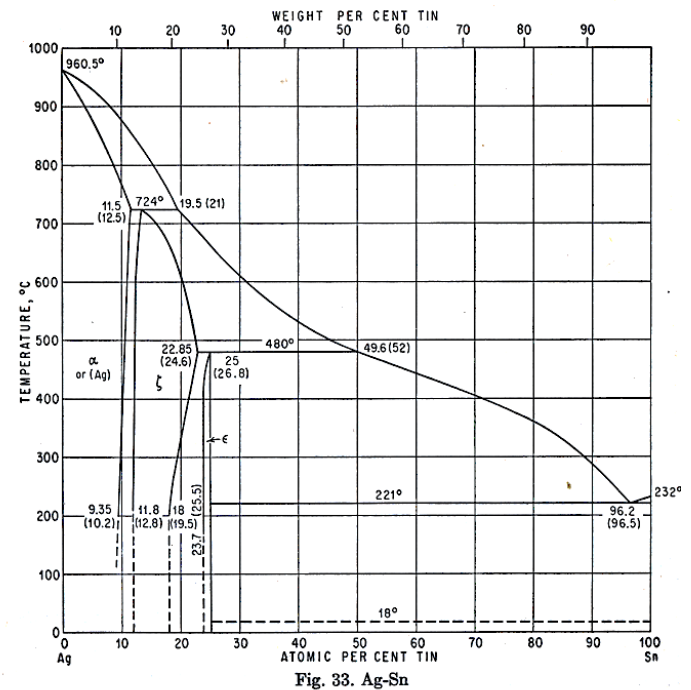


Figure 7: Silver/Tin Phase Diagram [3,4]

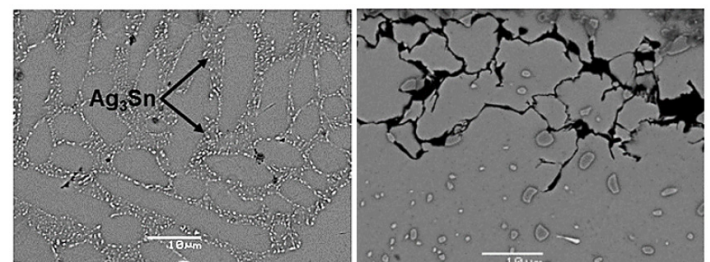


Figure 8: Backscattered scanning electron micrographs illustrating Ag_3Sn IMC Phase in SAC305: As Solidified (left), After Thermal Cycling [8]

Gold IMC In SnPb and SAC Solder Alloys

Gold plating is used as a solderable surface finish for both components and printed circuit boards in the electronics industry for decades. Gold is primarily plated over nickel, to prevent the formation of nickel oxide which has extremely poor solderability characteristics. Gold surface finish plating provides three distinct attributes: (1) gold is an excellent electrical contact surface due to its low electrical resistance and good solderability, (2) gold does not form an oxide layer which leads to maintenance of excellent solderability during storage, and therefore is often considered the optimal surface finish for printed circuit board and components in long-term storage, and (3) gold is used as a sacrificial surface finish rather than a primary solder finish, as it dissolves into the solder leaving behind a pristine surface of the underlying nickel layer to which the solder wets to and reacts, forming a solder-nickel interface in the solder joint. Figure 9 depicts the tin/gold phase diagram shows solubility of Au in Sn of less than 0.3 wt. % from room temperature to 200°C.

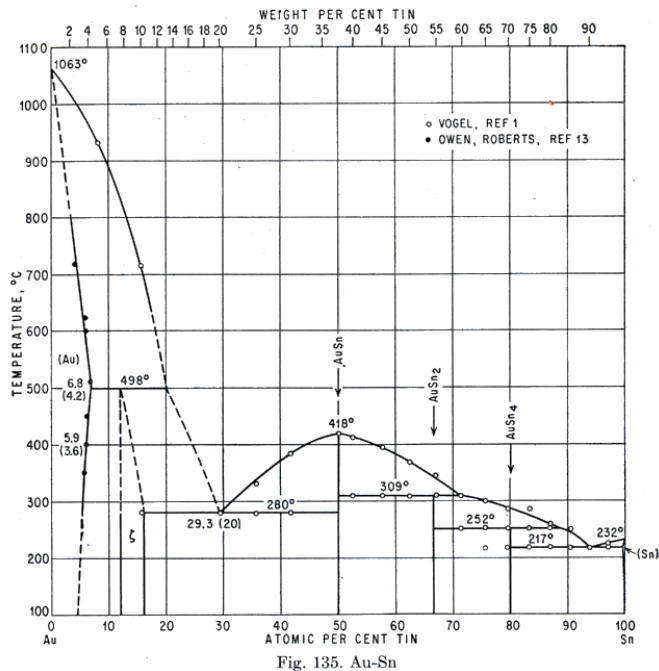


Figure 9: Gold/Tin Phase Diagram [3,4]

Bader documented the dissolution rate of gold into a 60Sn40Pb solder alloy recording a dissolution rate of approximately 1 μm/second at 200°C [9]. Hillman et al. documented the dissolution rate of gold in SAC305 solder of approximately 6 μm/second at 250°C [10]. Figure 10 and Figure 11 show the differences of gold dissolution rate compared with other metals in SnPb and SAC305 solder alloys. The high solubility and fast dissolution rates of gold in molten solder make it well suited as a sacrificial surface finish for both SnPb and Pb-free soldering processes.

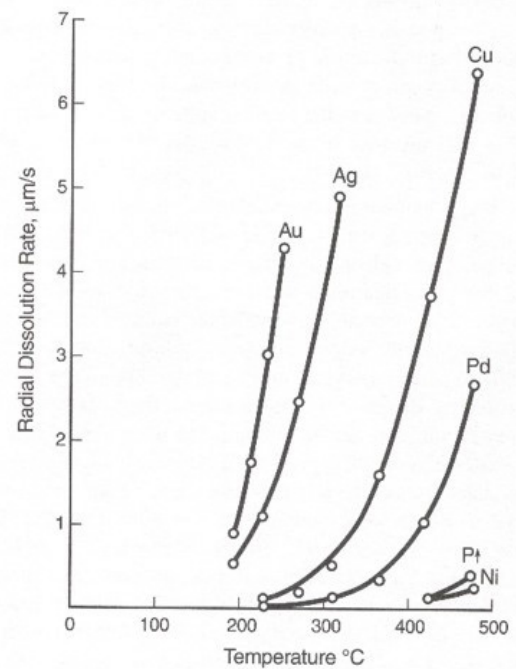


Figure 10: Dissolution Rates of Various Elements in 60Sn40Pb Solder [9]

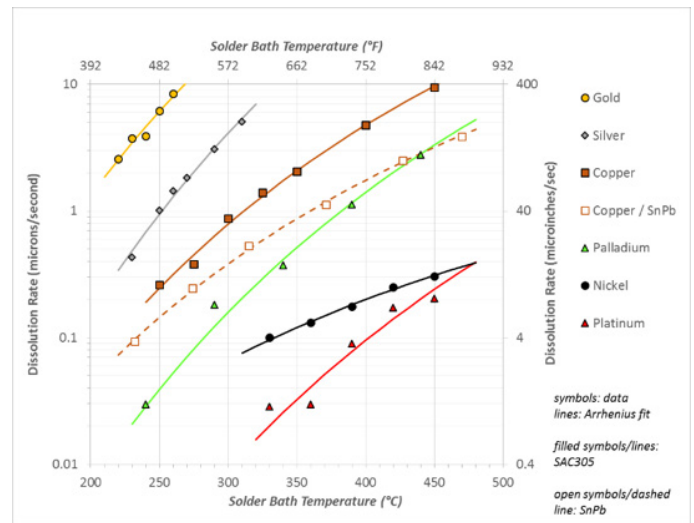


Figure 11: Dissolution Rates of Various Elements in SAC305 Solder compared with Cu dissolution into SnPb [10] Note that the vertical scale (dissolution rate) is a log scale

The AuSn₄ IMC phase forms as high-aspect ratio platelets in solder joints. Figure 12 illustrates the AuSn₄ morphology as a platelet structure in a SnPb solder joint. When the gold concentration in the solder joint exceeds approximately 3-5% by weight, the elongated platelets form and influence the solder joint reliability. Figure 13 is a scanning electron microscopy image showing AuSn₄ IMC platelets.

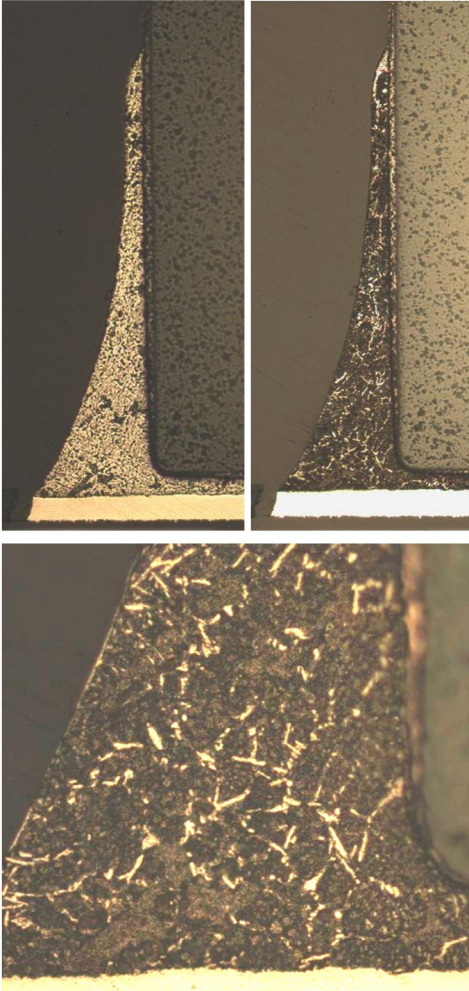


Figure 12: Optical photomicrograph of a solder joint containing AuSn_4 IMC phase (white platelets). Upper left, as polished, Upper right, Carapella's reagent, Lower center - higher magnification of etched sample (Photos courtesy of Collins Aerospace).

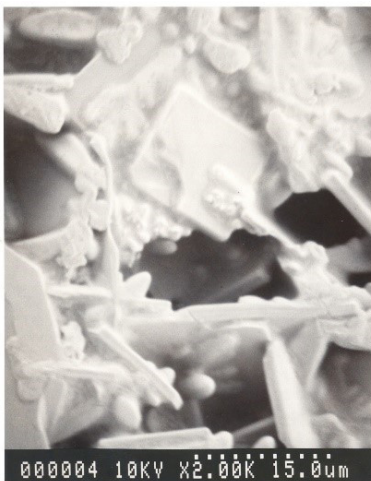


Figure 13: Scanning electron microscopy image of etched Sn-Pb solder joint containing AuSn_4 IMC platelets (Photo courtesy of Collins Aerospace)

The origin of the 3-5wt% Au limit comes from Bester who conducted IZOD impact testing demonstrating the effect of the amount of gold/tin intermetallic phase on the solder joint integrity as a function of the gold content of the solder joint up to 10 wt.% Au [11]. As shown in Figure 14, Bester's test results show a pronounced IZOD test data impact, with compositions less than approximately 4 wt.% Au content show a small drop in performance but with a pronounced drop in performance at 5wt% Au. These results demonstrated that a small fraction of AuSn_4 platelets in the solder joint microstructures (below 3-4wt% Au) do not degrade the solder joint integrity as measured by impact testing. Solder joint integrity degrades in the 3- 5wt% Au range.

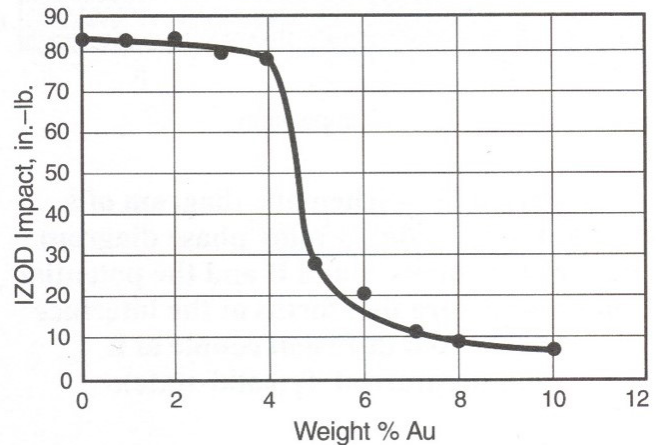


Figure 14: Bester's IZOD impact test data as a function of gold concentration [11]

Palladium IMC In SnPb and SAC Solder Alloys

Palladium and tin form a brittle intermetallic phase in both SnPb and SAC solder alloys, PdSn_4 , which causes the degradation of solder joint integrity in a similar mode as gold/tin IMC phases. The PdSn_4 phase forms as platelets in the solder joint when the palladium concentration in the solder joint exceeds approximately 0.3%-1.0% by weight (Figure 15). The primary difference between palladium and gold is the diffusion rate into molten solder. As shown in Figure 11, the dissolution rate of palladium is orders of magnitude slower than gold and can potentially result in an increased risk of embrittlement. Industry investigations [12, 13, 14] have reported the formation of the brittle PdSn_4 intermetallic phase for palladium plating thicknesses in the 20-30 microinch range. Palladium finishes with thicknesses less than 20 micro inches have been shown not impact solder joint thermal cycle integrity [12, 15].

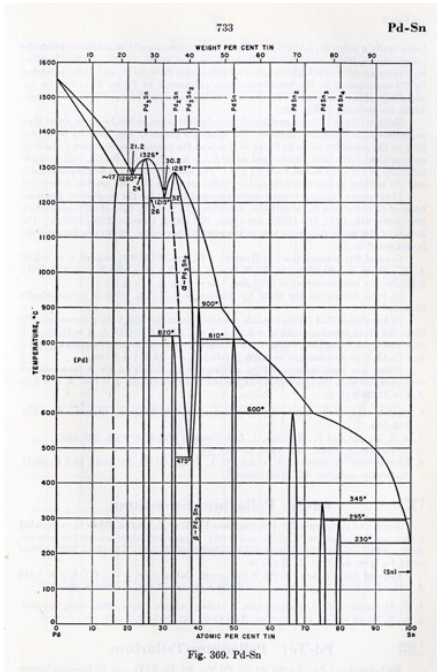


Figure 15: Palladium/Tin Phase Diagram [3,4]

IMCS IN GENERATION 3 LEAD-FREE SOLDER ALLOYS

Metallurgical Considerations

The addition of Ag strengthens Sn and improves the creep resistance of the SAC solder by precipitation hardening as illustrated in Figure 8. The addition of other alloying elements can improve the creep resistance of the solder by means of two other well-known metallurgical strengthening mechanisms, solid solution hardening and dispersion hardening. The introduction of solute atoms into solid solution of a solvent-atom lattice invariably produces an alloy that is stronger than the pure metal [16]. Figure 16 shows a simplified schematic illustration of substitutional solid solution strengthening. Substitutional or interstitial solute atoms strain the lattice and dislocation movement, or deformation is inhibited by interaction between dislocations and solute atoms incorporated into the β -Sn lattice.

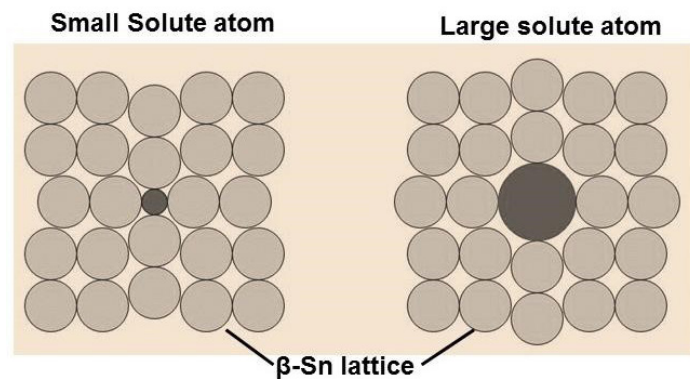


Figure 16: A simple schematic illustrating lattice distortion due to substitutional solute atoms.

If solute atoms precipitate from solution during thermal excursions in service, the solder alloy may strengthen subsequently due to dispersion hardening. Dispersion strengthening occurs when insoluble particles are finely dispersed in a metal matrix. Typical dispersion strengthened alloys employ an insoluble, incoherent second phase that is thermally stable over a large temperature range (Figure 17) [17]. For Sn-based solder alloys, the strength would be derived from a combination of increased solid solution strengthening at higher temperatures due to increased solubility, and dispersion strengthening that would supplement the solid solution effect at lower temperatures where solubility has decreased.

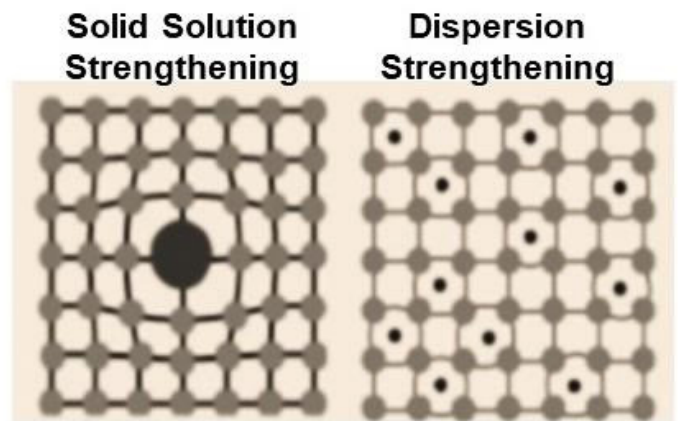


Figure 17: A simple schematic illustrating solid solution (left) and dispersion strengthening (right).

The development of Innolot provides evidence that substitutional solid solution strengthening can improve resistance to creep and fatigue at higher temperatures in Sn- based, Pb-free solders [18]. The current working hypothesis is that solid solution and dispersion strengthening not only supplement the Ag_3Sn precipitate hardening found in SAC solders but continue to be effective once precipitate coarsening reduces the effectiveness of the intermetallic Ag_3Sn precipitates [19].

The elements proposed most for improving elevated temperature properties in Sn-based, third generation solders are Bi, Sb and In. Bi and In, when used as a major alloying elements, also reduce the melting point of most solder alloy formulations, while the addition of Sb tends to increase the melting point [20]. These modified SAC alloys are off-eutectic compositions and are characterized by non-equilibrium solidification and often significant melting ranges [21-23].

Antimony (Sb) Additions to Tin (Sn)

The binary Sn-Sb phase diagram in Figure 18 shows solubility of Sb in Sn of approximately 0.5 wt. % at room temperature to 1.5 wt. % at 125°C. Thus, some contribution is expected from solid solution strengthening due to Sb dissolved in Sn-based Pb-free solders [18].

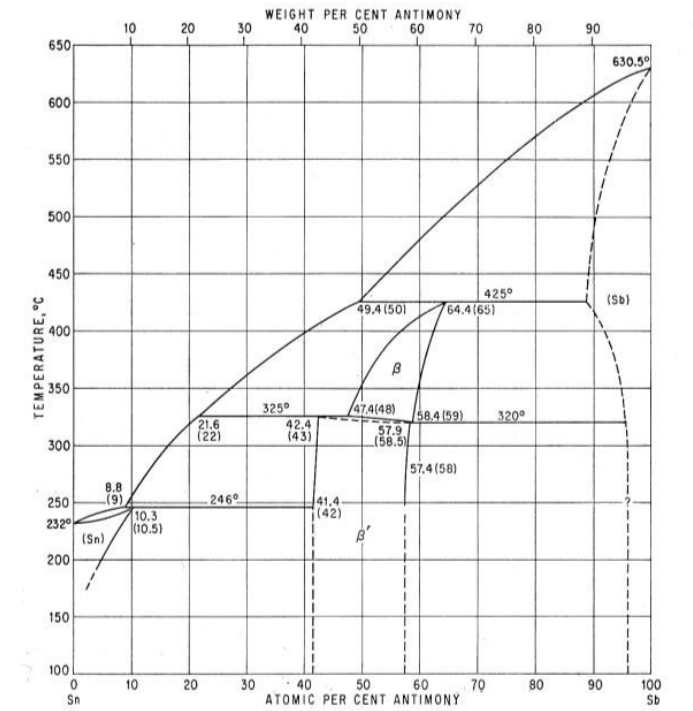


Figure 18: The Sn-Sb binary phase diagram [3,4]

Alloying with Sb may improve performance through other strengthening mechanisms. Studies by Li et al show that Sb slows the growth rate of Cu_6Sn_5 intermetallic compound (IMC) layers at attachment interfaces [24, 25]. Fast interfacial IMC growth on Cu surfaces tends to produce irregular and non-uniform IMC layers. This can lead to reduced mechanical reliability by inducing fractures at IMC interfaces or through the IMC in drop/shock loading [26].

Figure 18 also shows that Sb has the potential to form multiple different intermediate phases or IMCs with Sn (Sb_2Sn_3 , SbSn , Sb_4Sn_3 , Sb_5Sn_4 , and SbSn_2) in the bulk solder. Lu et al [27] and El-Daly et al [28] identified SnSb intermediate phase precipitates $<5\mu\text{m}$ in size and distributed throughout the Sn dendrites. Beyer et al show that Sn5Sb and Sn8Sb alloys have increased shear strength and ductility compared to conventional SAC solders and maintain their shear strength with good ductility after isothermal aging [29]. El-Daly suggests Sb also can improve creep performance and tensile strength [30]. In this case, the SbSn precipitates form within the Sn dendrites, unlike the well-known SAC Ag_3Sn mechanism, where the precipitates form at the Sn dendrite boundaries. The SbSn precipitates work to resist recrystallization by strengthening the Sn dendrites [16].

Indium (In) Additions to Tin (Sn)

The binary Sn-In phase diagram is shown in Figure 19. While there is disagreement over the solid solubility of In in Sn, a reasonable estimate is ~ 7 wt. % at room temperature and as much as 12 wt. % at 125°C [3,4]. Because of its range of solubility in Sn, In has been explored as a solid solution strengthening agent in Sn-based Pb-free solders [31-32]. The equilibrium diagram shows that

In forms two intermediate phases (β and γ) of variable composition with Sn [3,4] but does not appear to form any true stoichiometric compounds with Sn.

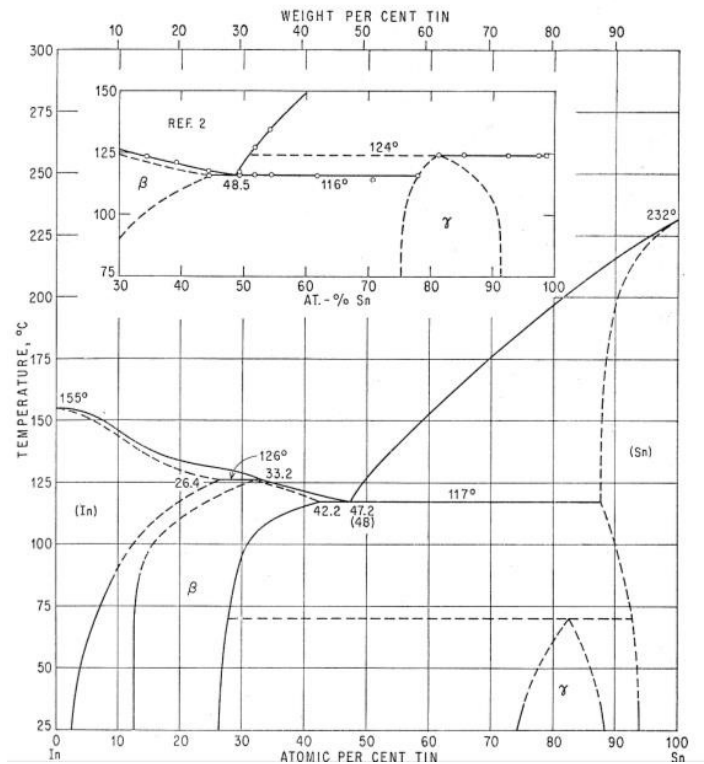


Figure 19: The In-Sn binary phase diagram [3,4]

Results from multiple solder alloy studies indicate that In additions can improve drop and shock resistance by slowing the growth of interfacial IMC layers. Yu et al report improved drop [33] and thermal shock [34] performance by adding as little as 0.4% In, and Amagai et al report improved drop performance at or below 0.5% In [35]. Hodúlová et al In slows growth of Cu_3Sn and that a hybrid IMC phase $\text{Cu}_6(\text{Sn}, \text{In})_5$ forms [36]. Sharif also observed the formation of the $\text{Cu}_6(\text{Sn}, \text{In})_5$ IMC as well as formation of $(\text{Cu}, \text{Ni})_3(\text{Sn}, \text{In})_4$ on Ni substrates [37], and these IMCs also could be found in the bulk as well as the interfaces. In these hybrid IMCs, In substitutes for Sn which fundamentally is different than the common modified IMCs $(\text{Cu}, \text{Ni})_6\text{Sn}_5$ or the $(\text{Ni}, \text{Cu})_3\text{Sn}_4$ where Cu and Ni exchange.

Other reactions can occur when In is added to SAC-based solders, and this complicates the ability to understand the effect of In content on solder joint reliability. In a study by Chantaramance et al additions of 0.5% In or Sb in combination with In was found to promote formation of $\text{Ag}_5(\text{Sn}, \text{In})$ and SnSb [38]. They reported that small precipitates reduced the Sn dendrite size by 28%, but they were unable to determine the relative influence of In versus Sb on this reaction. With alloys containing In of the order of 10%, Sopoušek et al found that some of the Ag_3Sn transforms to $\text{Ag}_2(\text{Sn}, \text{In})$ and Ag_2Sn [39]. These observations are consistent with the Ag-Sn binary phase diagram that shows Ag_3In , Ag_2In , and AgIn_2

[17]. Wang et al reported that an addition of 1% In caused larger or coarser Ag₃Sn precipitates [40]. This is an interesting observation, since Ag₃Sn precipitate coarsening (larger precipitates at time zero) could reduce thermal cycling reliability. In principle there is a large solid solubility of In in Sn, but the effective In content in a SAC-based solder may be diminished by interactions with other elements to form multiple phases.

It is noteworthy that many of the studies were conducted using laboratory bulk solder samples with microstructures that are likely to be atypical of microelectronic solder joints. Some of the studies also included more than one significant alloy addition [e.g., 38], which makes it difficult to isolate effects due to individual alloying elements. The work by Wada et al [31,32], while it includes tensile testing with comparatively large, bulk samples, also includes thermal cycling and drop testing with surface mount components. Their microstructural analysis included X-ray diffraction and they found InSn₄, In₄Ag₉, Ag₃(Sn, In), and possibly αSn in addition to βSn. Wada concluded that the optimum ductility and reliability was achieved with an In content of 6 wt. %.

Bismuth (Bi) Additions to Tin (Sn)

The binary Sn-Bi phase diagram is shown in Figure 20. The solubility of Bi in Sn is approximately 1.5 wt. % at room temperature and increases to almost 7 wt. % at 100°C room temperature, and as much as 15 wt. % at 125°C [3,4]. There is almost no solubility of Sn in Bi, and no intermediate phases or IMC are found in the Sn-Bi system.

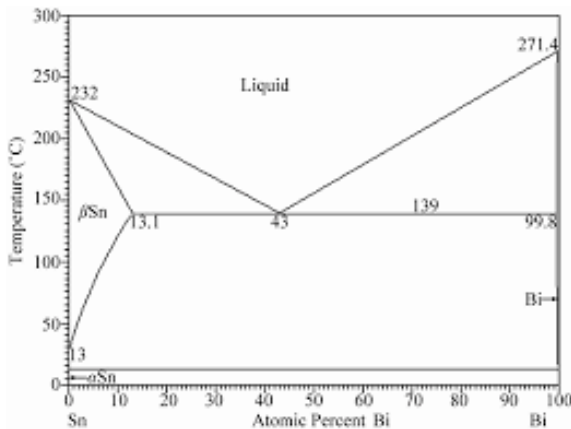


Figure 20: The Sn-Bi binary phase diagram [3,4]

Multiple studies have shown that Bi improves the mechanical properties of Sn and SAC solders [41, 18, 19, 42-54]. Vianco [42,43] and Witkin [46, 50-52] have done extensive mechanical testing and microstructural analysis and discuss the dual strengthening mechanisms of Bi in solid solution and Bi precipitated within Sn dendrites and at Sn boundaries. Recently, Delhaise et al [53] reported results from their study of the effects of thermal preconditioning (aging) on microstructure and property improvement in an alloy containing 6 wt. % Bi. They suggest that strain from Bi precipitation induces recrystallization and an increase in the amount of Sn grain boundaries which in turn, are pinned by the Bi precipitates at those

boundaries. These microstructural features work in conjunction with Bi in solid solution to resist creep deformation.

The results from the fundamental studies by Vianco [42,43] and Witkin [46, 50, 51] leave no doubt that Bi additions can have a positive effect on the physical properties of Sn and Sn-based solder alloys. However, those studies used cast, bulk alloy samples and it is debatable if those results can be scaled effectively to smaller, microelectronic solder joints. Nishimura et al for example, recommend a maximum Bi content of only 1.5 wt. % (Figure 21a) because of the uncertainty that the alloying effect will be sustained as the microstructure evolves in response to the thermal cycling in normal service [48]. Delhaise has shown that the Bi distribution and microstructure depend on solidification conditions and subsequent thermal exposure, which determine the relative contributions of Bi to solid solution and dispersion strengthening (Figure 21b).

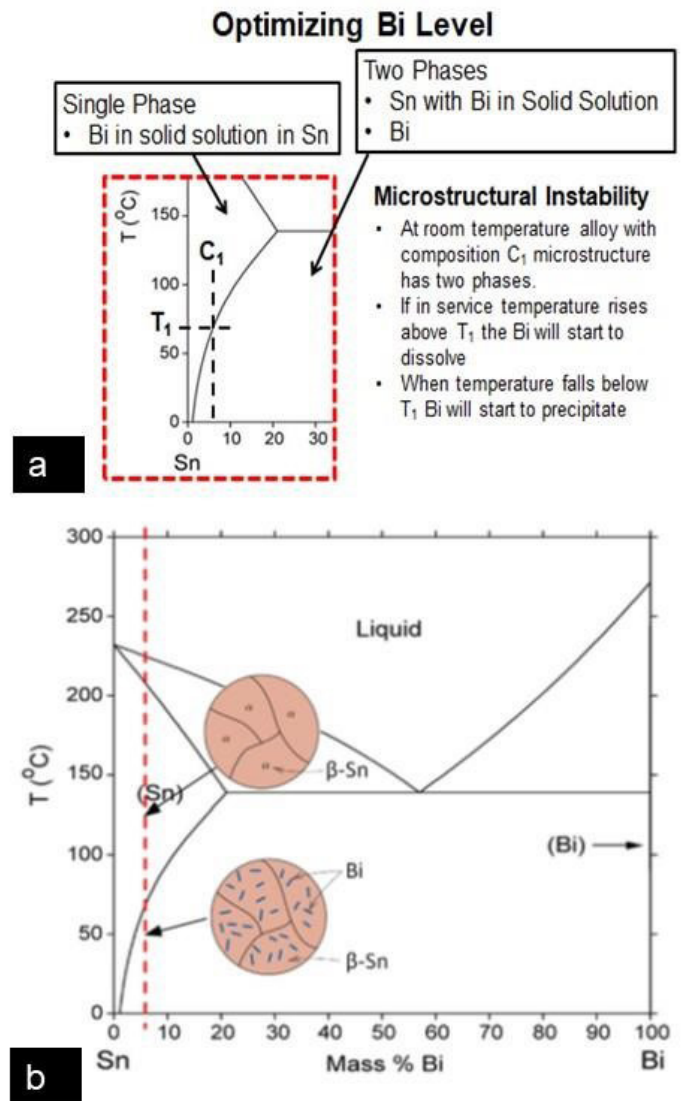


Figure 21: Emphasis on the Sn-rich regions of the Sn-Bi binary phase diagram showing: a) Factors to consider when for optimizing the Bi level, courtesy, K. Sweatman [54], and b) Microstructures shown schematically for solid solution (upper) and dispersion strengthening (lower) with the 6 wt. % Bi alloy (Violet), from Delhaise [53].

Furthermore, it is possible that adding enough Bi to take advantage of the Bi solubility limit at higher temperatures may have a negative effect because Bi does not always precipitate homogeneously. Clustering of Bi is known to occur [53] and in the extreme case, stratification or segregation may induce brittle behavior [55,56]. The current experimental test plan offers the opportunity to explore the stability of the Bi content in the 6 wt. % Bi alloy (Violet) alloy using thermal cycling at upper temperature extremes of 100 °C and 125 °C.

These intermetallic precipitates are recognized as the primary strengthening mechanism in SAC solders [57, 58, 42, 43]. During thermal or power cycling and extended elevated temperature exposure, the Ag_3Sn precipitates coarsen and become less effective in inhibiting dislocation movement and slowing damage accumulation. This pattern of microstructural evolution is characteristic of the thermal fatigue failure process in these Sn-based Pb-free alloys and was described originally in detail by Dunford et al in 2004 [20]. Figure 8 shows scanning electron micrographs illustrating coarsening of the Ag_3Sn precipitates in SAC305 solder caused by thermal cycling.

DISCUSSION

It would be incorrect to state that the various IMC phases described in the paper are not associated with solder joint reliability issues. However, the emphasis on the impact of IMC phases on solder joint is clearly overstated in the electronic industry. The following five case studies document validated IMC defect root cause examples.

Case #1: Literature Investigations

The authors review 1, 549 papers in the Journal of Electronic Materials and 951 papers in the IEEE Xplore publication databases looking for publications on product or field failures relating to IMC phases are the failure root cause. Only two published papers were found: (1) C. Lim et al., “Failure Characterization of BGA Solder Joint Fracture During Field Application” which concluded the solder joint failure was due to excessive IMC thickness due to multiple reflow cycles [59]; (2) Y. Mo et al., “Failure Analysis on the BGA Solder Joint” which concluded that the solder joint failure was due to irregular 25.75 μm IMC thickness [60].

Case #2: Microcracking of Copper/Tin IMC Phases Impacting Specific Product Applications

Hodolova et al found that the Cu_6Sn_5 IMC phase developed micro-cracks at the IMC phase after oven thermal aging from 130C - 170C for 2-16 days and thermal cycle conditioning [7]. These micro-cracks illustrated brittleness of the IMC phase, but overall degradation of the solder joint would require significant mechanical deformation. Their work also demonstrated that the constituent additions of bismuth and indium impacted the IMC phase growth rates and decreased the overall rated of IMC phase micro-cracking. Similarly, K Sweatman et al, investigated the influence of nickel and reflow profile parameters on the microcracking of the Cu_6Sn_5 IMC phase [61,62]. The microcracking observed in the solder joints would not be considered a major reliability issue but could pose a

solder joint cracking risk in certain specific commercial product applications.

Case #3: Assembly Failure Due to Improper Maintenance

The introduction of SAC soldering processes resulted in significant changes to wave solder and selective solder equipment due to the increased dissolution properties of SAC solder in comparison to SnPb solder. The solder pots containing the molten SAC solder alloy required either a protective coating or be constructed of a dissolution resistant metal such as titanium. Solder pots made from iron-based metals could be significantly damaged due to dissolution of the iron by the molten solder resulting in the formation of iron/tin IMC needle-like structures. A review of the iron/tin phase diagram shows that two intermetallic compounds (IMCs) can be formed – FeSn or $FeSn_2$ which are not wettable by solder. D. Barbini [63] documented the formation of $FeSn_2$ IMC structures due to the increased dissolution capacity of lead-free solders. $FeSn_2$ IMC structures have a higher density than molten tin/lead or lead-free solder; therefore, if they form, they will sink to the bottom of a wave solder pot, which results in their accumulation and damage to the wave solder pot impellers without proper maintenance. Figure 22 illustrates a wave solder pot accumulation of $FeSn_2$ IMC structures. Manko [64], Schlessmann [65], and Diepstraten & Trip [66] all documented similar formations of $FeSn_2$ IMC structures due to dissolution of iron from a wave solder pot.

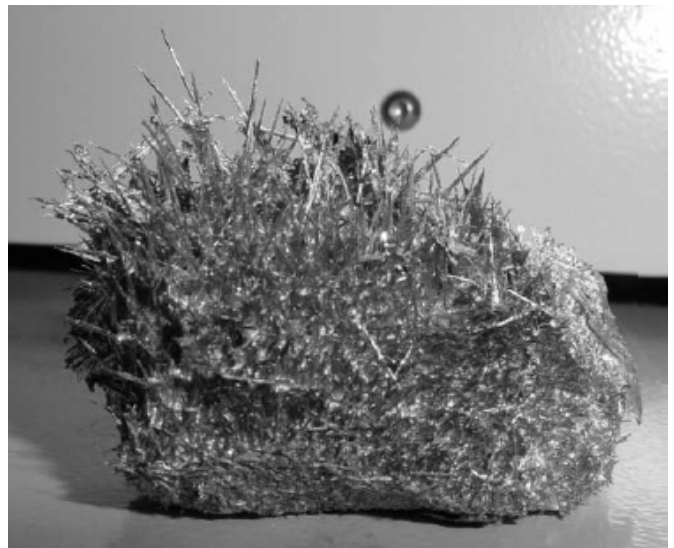


Figure 22: $FeSn_2$ IMC Structure Due To Solder Pot Damage [63]

Cookson Electronics documented an identical analysis of $FeSn_2$ IMC due to excessive preventative maintenance of a tin/lead wave solder process [67]. Overly aggressive scraping of the wave solder pot during dross removal was found to have damaged the wave solder pot protective coating, which allowed for the dissolution of iron and the formation of the $FeSn_2$ IMCs. The $FeSn_2$ IMC structures were then transferred by the molten solder forming bridged solder joints on printed wiring assemblies (see Figure 23).

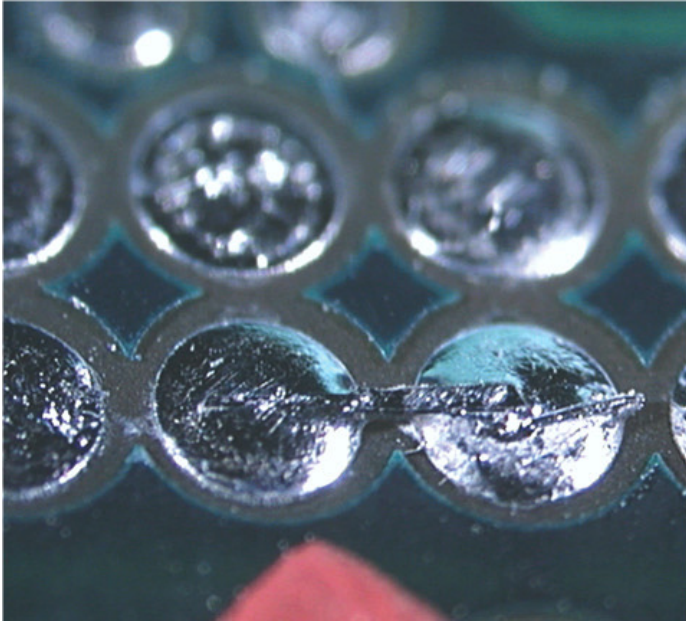


Figure 23: FeSn₂ IMC Phase Solder Defect [67]

Improper maintenance of SnPb wave solder and selective solder equipment is not immune from the possible impact of FeSn₂ IMC phase defects. Figure 24 illustrates a similar defect root cause for a SnPb wave solder system where the FeSn₂ IMC phase formation resulted in the shorting of solder joints [6]. Scanning electron microscopy identified the IMC phase as FeSn₂ (Figure 25).



Figure 24: FeSn₂ IMC Phase Shorting Defect

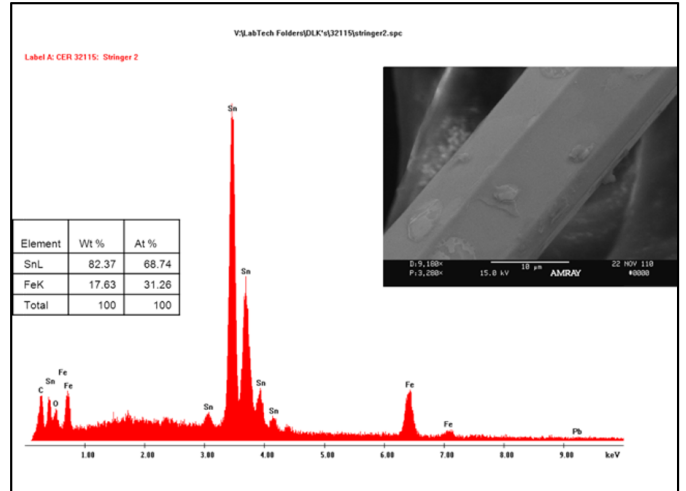


Figure 25: SEM Identification of the IMC Phase as FeSn₂

Case #4: Tin/Copper IMCs Masquerading as Tin Whiskers - Inadequate Tinning Pot Protocols

The implementation of the Restriction of Hazardous Substances (RoHS) European Union (EU) Directive in 2005 resulted in the introduction of pure tin as an acceptable surface finish for printed circuit boards and component terminations. A drawback of pure tin surface finishes is their potential to form tin whiskers. The tin whisker metallurgical phenomenon is associated with tin rich/pure tin materials and has been a topic of intense industry interest [68-73]. Figure 26 illustrates tin whiskers observed on a component lead and in an immersion tin surface finished plated through hole that was incorrectly plated.

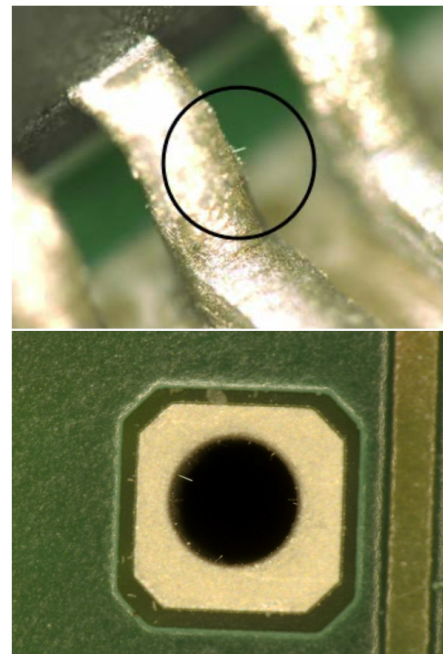


Figure 26: Tin Whiskers Observed on a Component Lead (top) and in a Plated Through Hole (bottom) [74]

As previously discussed, SnPb soldering processes result in the formation of the Cu_6Sn_5 IMC phase which can be observed distributed around the solder joint microstructure as needles. The Cu_6Sn_5 intermetallic needles have a hollow, hexagonal geometry. One industry failure analysis documented a case of mistaken identity of tin whiskers and copper/tin IMCs. The inspection of a printed circuit assembly revealed tin whiskers on a quad flat pack (QFP) component (Figure 27).

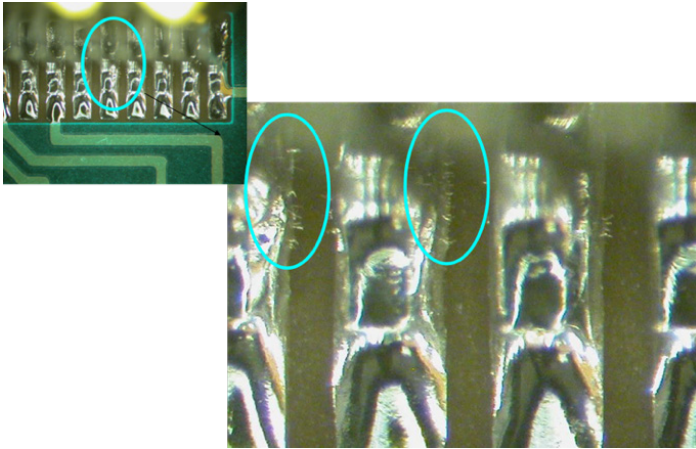


Figure 27: Observed Structures on QFP Component

Scanning electron microscopy (SEM) analysis results revealed the identity of the whisker-like anomalies observed on the QFP component. The SEM EDX results show a copper/tin element ratio of the anomalies to be approximately six parts copper to five parts tin which would correspond to the Cu_6Sn_5 tin/copper IMC phase [75]. The Cu_6Sn_5 tin/copper IMC phase forms in a needle morphology as the copper content of the solder begins to exceed approximately 0.3% [76, 1]. The Cu_6Sn_5 intermetallic needles often form and grow preferentially from component lead and/or printed wiring pad edges. Figures 28 and 29 illustrate the QFP defects observed during SEM analysis. A review of the QFP component history revealed that QFP component was not placed during automated assembly process due to a lack of QFP component availability. The QFP was manually soldered by an operator. Further investigation of the operator's QFP soldering procedure did not reveal any unusual or incorrect soldering technique or procedure. It is hypothesized that original QFP tin/lead surface finish contained higher than normal copper content and the manual soldering operation resulted in the formation of the Cu_6Sn_5 tin/copper intermetallic needles. A solder wick and re-soldered process was conducted on QFPs that exhibited the Cu_6Sn_5 tin/copper intermetallic needles and no reoccurrence of the Cu_6Sn_5 tin/copper intermetallic needles was observed after completion of the process.

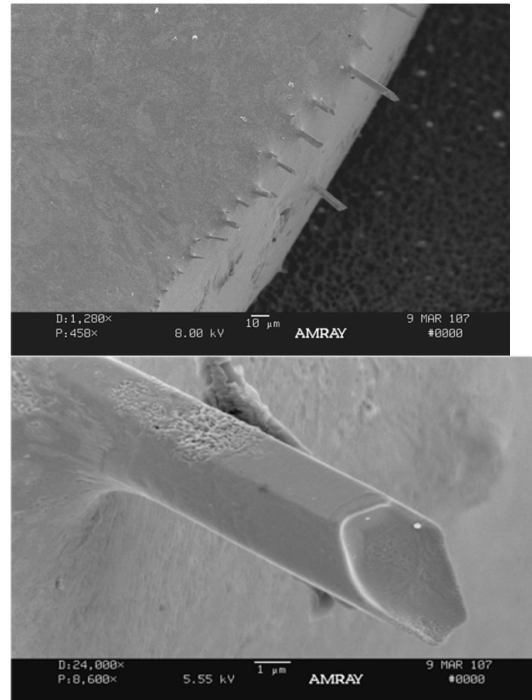


Figure 28: Scanning Electron Microscopy Image of Cu_6Sn_5 IMC Phase As Soldered

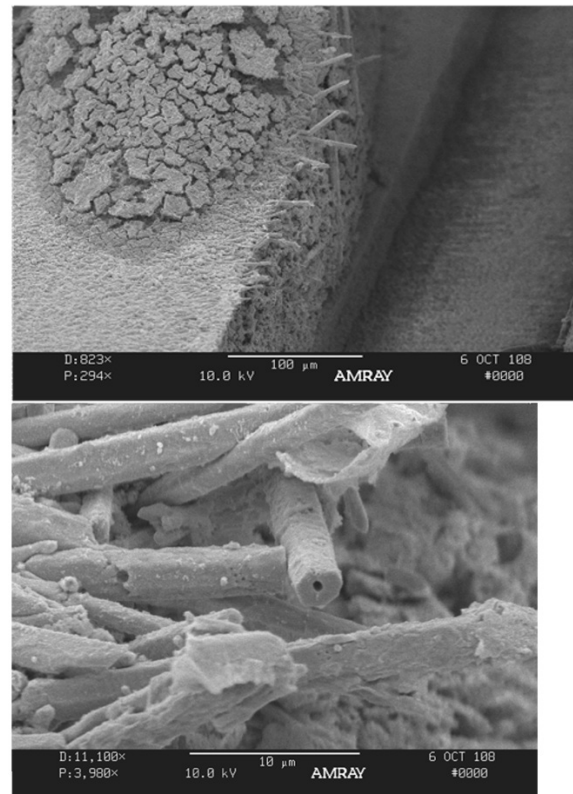


Figure 29: Scanning Electron Microscopy Image of Cu_6Sn_5 IMC Phase After Etching

Case #5: Improper Rework Processes Impacting Copper/Tin IMC Phases

Excessive IMC phase formation is typically the result of improper soldering or rework/repair processes. Excessive soldering temperatures or soldering dwell times allows the formation of thick IMC phase thicknesses at the expense of the printed circuit board component pad. Figure 30 illustrates the impact of five rework operations on a BGA component resulting in the excessive copper/tin IMC and dissolution of the BGA pad. Figure 31 illustrates a more severe case of BGA improper rework where the component copper pad is nearly eliminated due to dissolution by the SAC solder alloy. The severe damage to the component copper pad could result in solder joint cracking, pad cracking or pad delamination from the printed circuit board laminate under mechanical stress or fatigue conditions.

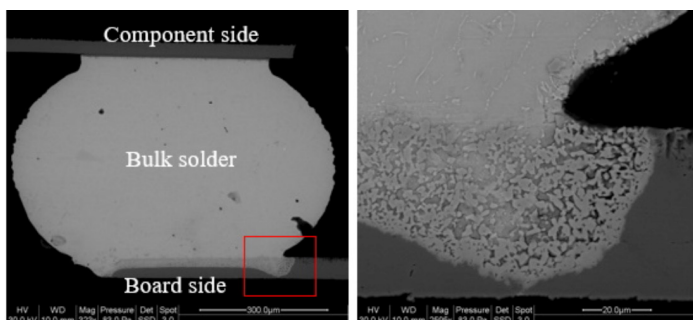


Figure 30: Excessive Copper/Tin IMC Formation At BGA Copper Pad After 5 Rework Operations [Photos courtesy of CALCE]

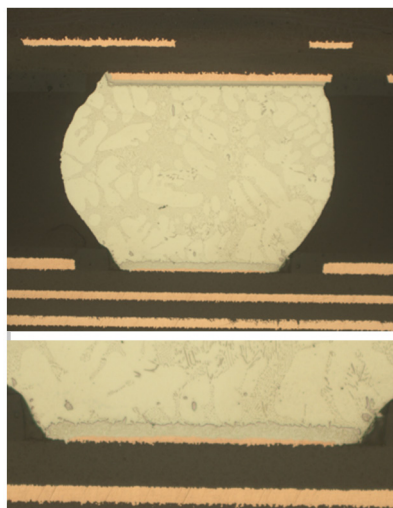


Figure 31: Excessive BGA Component Rework Resulting In Near Complete Pad Dissolution/Excessive IMC [77]

The electronics industry focus on the IMC phases/IMC thicknesses results in misinterpretation of solder joint failures and root cause corrective action. The root causes of the discussed detailed cases revealed a wide range of issues: improper maintenance, excessive rework procedures, inadequate tinning pot protocols, specific high strain commercial product application and incorrect/inadequate

soldering processes. The industry emphasis should be on better soldering processes, rigidly controlled rework protocols and detailed focus failure analysis. The industry data demonstrates that brittle IMC phases should not be a primary concern for solder joint reliability. Vianco's summary of the influence of the IMC phase on solder joint reliability is a perfect summary: "...the propensity for failure to occur in the IMC layer depends upon the following factors: (1) the strength of the solder alloy; (2) the rate at which a load is applied to the joint (relating to the strain rate sensitivity of the solder alloy); (3) the brittleness of the IMC layer composition; (4) the thickness of the IMC layer." [1]. Over emphasis of IMC phase as a primary solder joint reliability issue only consumes cost/time resources with no contribution of problem resolution.

CONCLUSION

The emphasis on the influence of IMC phases on solder joint reliability in the electronics industry is clearly overstated and often excessive. A review of industry publications/cases clearly shows that solder joint reliability is impacted by IMC phases with root causes of incorrect soldering processes or inadequate process procedure. The list of solder joint reliability root cause failures should not include IMC phases as a primary solder joint failure mode.

REFERENCES

1. P. Vianco, Soldering Handbook, 3rd Edition, American Welding Society, ISBN 0-87171-618-6
2. P. Ratchev et al, "A Study of Ductile to Brittle Fracture Transition Temperatures in Bulk Pb free Solder Alloys," EMPC 2005, Brugge, Belgium
3. Max Hansen, Constitution of Binary Alloys, 2nd edition, McGraw-Hill, 1175-1177, 1958.
4. Rodney P. Elliot, Constitution of Binary Alloys, First Supplement, McGraw-Hill, 802, 1965.
5. P. Vianco, et al, Solid State Intermetallic Compound Layer Growth Between Copper and SAC Solder," Journal of Electronic Materials, Vol. 33, No. 9, September 2004]
6. D.Hillman, unpublished manuscript
7. E. Hodulova, et al, "Structural Changes of the IMC in Lead Free Solder Joints," Materials Transactions, Vol. 56, No. 7, 2015.
8. R. Coyle et al, "The effect of bismuth, antimony, or indium on the thermal fatigue of high reliability Pb- free solder alloys," SMTA International Conference, 2018.
9. W. Bader, "Dissolution of Au, Ag, Pd, Pt, Cu, and Ni in a Molten Tin-Lead Solder," Welding Journal 48, 1969.
10. D. Hillman et al, "Dissolution Rate of Electronics Packaging Surface Finish Elements in Sn3.0Ag0.5Cu Solder", Journal of Electronic Materials, No. 48, 2019.
11. M. Bester, "Metallurgical Aspects of Soldering Gold and Gold Plating," InterNEPCON Proceedings, 1968.
12. I. Artaki et al, "Assessment of Nickel-Palladium Finished Components for Surface Mount Assembly Applications", SMTAI Conference Proceedings, 1995.
13. D. Hillman et al, "Wirebondability and Solderability of Various Metallic Finishes for Use in Printed Circuit Assembly, SMTAI Conference Proceedings, 1996.

14. A. Mei and A. Eslambolchi, "Evaluation of Ni/Pd/Au as an Alternative Metal Finish on PCB", SMTAI Conference Proceedings, 1998.
15. D. Hillman et al, "JCAA/JGPP No-Lead Solder Project: -55C to +125C Thermal Cycle Testing Final Report", Navy Mantech Contract GST 0504BM3419-02, March 2006.
16. G. E. Dieter, Mechanical Metallurgy, Chapter 5, "Plastic Deformation of Polycrystalline Aggregates, Solid Solution Hardening," 128, McGraw-Hill, 1961.
17. Peter Haasen, Physical Metallurgy, 3 Edition, Cambridge University Press, 375-378, 1996.
18. Anton-Zoran Miric, "New Developments In High-Temperature, High-Performance Lead-Free Solder Alloys," SMTA Journal, Volume 23, Issue 4, 24-29, 2010.
19. André Delhaise, Leonid Snugovsky, Doug Perovic, Polina Snugovsky, and Eva Kosiba, "Microstructure and Hardness of Bi-containing Solder Alloys after Solidification and Ageing," SMTA J., Vol. 27, issue 3, 22-27, 2014.
20. S. Dunford, S. Canumalla, and P. Viswanadham, "Intermetallic Morphology and Damage Evolution Under Thermomechanical Fatigue of Lead (Pb)-Free Solder Interconnections," Proceedings of Electronic Components Technology Conference, 726-736, Las Vegas, NV, June 1-4, 2004.
21. "Lead-Free Solder Project Final Report," NCMS Report 0401RE96, Section 2.4, Properties Assessment and Alloy Down Selection, National Center for Manufacturing Sciences, Ann Arbor, MI, May 1997.
22. T. Siewert, S. Liu, D. R. Smith, and J. C. Madeni, "Database for Solder Properties with Emphasis on New Lead-Free Solders: Properties of Lead-Free Solders Release 4.0," NIST and Colorado School of Mines, February 2002.
23. C. A. Handwerker, U. Kattner, K. Moon, J. Bath, and P. Snugovsky, "Chapter 1, Alloy Selection," in Lead-Free Electronics, 9-46, IEEE Press, Piscataway, NJ, 2007.
24. Li, G.Y., Chen, B.L., Tey, J.N., "Reaction of Sn-3.5Ag-0.7Cu-xSb solder with Cu metallization during reflow soldering," IEEE Transactions on Electronics Packaging Manufacturing, vol. 27, no. 1, 77-85, 2004.
25. Li, G.Y., Bi, X.D., Chen, Q., Shi, X.Q., "Influence of dopant on growth of intermetallic layers in Sn-Ag-Cu solder joints," Journal of Electronic Materials, vol. 40, no. 2, 165-175, 2011.
26. Per-Erik Tegehall "Review of the Impact of Intermetallic Layers on the Brittleness of Tin-Lead and Lead-Free Solder Joints, Section 3, Impact of Intermetallic Compounds on the Risk for Brittle Fractures" IVF Project Report 06/07, IVF Industrial Research and Development Corporation, 2006.
27. Lu, S., Zheng, Z., Chen, J., Luo, F., "Microstructure and solderability of Sn-3.5Ag-0.5Cu-xBi-ySb solders," Proceedings 11th International Conference on Electronic Packaging Technology and High Density Packaging, ICEPT-HDP 2010, 410-412, 2010.
28. A.A. El-Daly, Y. Swilem and A.E. Hammad, "Influences of Ag and Au Additions on Structure and Tensile Strength of Sn-5Sb Lead Free Solder Alloy," J. Mater. Sci. Technol., vol.24, no. 6, 921-925, 2008.
29. H. Beyer, V. Sivasubramaniam, D. Hajas, E. Nanser, F. Brem, "Reliability improvement of large area soldering connections by antimony containing lead-free solder," PCIM Europe Conference Proceedings, 1069-1076, 2014.
30. A.A. El-Daly, Y. Swilem, A.E. Hammad, "Creep properties of Sn-Sb based lead-free solder alloys," Journal of Alloys and Compounds, vol. 471, 98-104, 2009.
31. T. Wada, K. Mori, S. Joshi, and R. Garcia, "Superior Thermal Cycling Reliability of Pb-Free Solder Alloy by Addition of Indium and Bismuth for Harsh Environments, Proceedings of SMTAI, 210-215, Rosemont, IL, Sep 2016.
32. T. Wada, S. Tsuchiya, S. Joshi, and R. Garcia, K. Mori, and T. Shirai, "Improving Thermal Cycle Reliability and Mechanical Drop Impact resistance of a Lead-free Tin- Silver-Bismuth-Indium Solder Alloy with Minor Doping of Copper Additive," Proceedings of IPC APEX, San Diego, CA, February 14-16, 2017.
33. A-M Yu, J-W Jang, J-H Lee, J-K Kim, M-S Kim, "Microstructure and drop/shock reliability of Sn-Ag-Cu-In solder joints," International Journal of Materials and Structural Integrity, vol. 8 no. 1-3, 42-52, 2014.
34. A-M Yu, J-W Jang, J-H Lee, J-K Kim, M-S Kim, "Tensile properties and thermal shock reliability of Sn-Ag- Cu solder joint with indium addition," Journal of Nanoscience and Nanotechnology, vol. 12, no. 4, 3655- 3657, 2012.
35. M. Amagai, Y. Toyoda, T. Ohnishi, S. Akita, "High drop test reliability: Lead-free solders," Proceedings 54th Electronic Components and Technology Conference, 1304- 1309, 2004.
36. E. Hodúlová, M. Palcut, E. Lechovič, B. Šimeková, K. Ulrich, "Kinetics of intermetallic phase formation at the interface of Sn-Ag-Cu-X (X = Bi, In) solders with Cu substrate," Journal of Alloys and Compounds, vol. 509, no. 25, 7052-7059, 2011.
37. A. Sharif, Y. C. Chan, "Liquid and solid state interfacial reactions of Sn-Ag-Cu and Sn-In-Ag-Cu solders with Ni-P under bump metallization," Thin Solid Films, vol. 504, no. 1-2, 431-435, 2006.
38. S. Chantaramanee, P. Sungkhaphaitoon, T. Plookphol, "Influence of indium and antimony additions on mechanical properties and microstructure of Sn-3.0Ag-0.5Cu lead free solder alloys," Solid State Phenomena, 266 SSP, 196-200, 2017.
39. J. Sopoúšek, M. Palcut, E. Hodúlová, J. Janovec, "Thermal analysis of the Sn-Ag-Cu-In solder alloy," Journal of Electronic Materials, vol. 39, no. 3, 312-317, 2010.
40. J.Wang, M. Yin, Z. Lai, X. Li, "Wettability and microstructure of Sn-Ag-Cu-In solder," Hanjie Xuebao/Transactions of the China Welding Institution, vol. 32, no. 11, 69-72, 2011.
41. Polina Snugovsky, Simin Bagheri, Marianne Romansky, Doug Perovic, Leonid Snugovsky, and John Rutter, "New Generation Of Pb-Free Solder Alloys: Possible Solution To Solve Current Issues With Mainstream Pb-Free Soldering," SMTA J., Vol. 25, issue 3, 42- 52, July 2012.
42. P.T. Vianco and J.A. Rejent, "Properties of Ternary Sn- Ag-Bi Solder Alloys: Part I - Thermal Properties and Microstructural Analysis," J. Electronic Materials, Vol. 28, no. 10, 1127-1137, 1999.

43. P.T. Vianco and J.A. Rejent, "Properties of Ternary Sn-Ag-Bi Solder Alloys: Part I - Wettability and Mechanical Properties Analyses," *J. Electronic Materials*, Vol. 28, no. 10, 1138-1143, 1999.
44. Jie Zhao, Lin Qi, Xiu-min Wang, "Influence of Bi on microstructures evolution and mechanical properties in Sn-Ag-Cu lead-free solder," *J. Alloys and Compounds*, Vol. 375, Issues 1-2, 196-201, July 2004.
45. Dave Hillman, Tim Pearson, and Ross Wilcoxon, "NASA DOD -55 °C to +125 °C Thermal Cycle Test Results," *Proceedings of SMTAI 2010*, 512-518, Orlando, FL, October 2010.
46. David Witkin, "Mechanical Properties of Bi-containing Pb-free Solders," *Proceedings IPC APEX 2013*, S11-01, San Diego, CA, February 2013.
47. Joseph M. Juarez, Jr., Polina Snugovsky, Eva Kosiba, Zohreh Bagheri, Subramaniam Suthakaran, Michael Robinson, Joel Heebink, Jeffrey Kennedy, and Marianne Romansky, "Manufacturability and Reliability Screening of Lower Melting Point Pb-Free Alloys Containing Bismuth," *J. Microelectronics and Electronic Packaging*, Vol. 12, no. 1, 1-28, 2015.
48. Takatoshi Nishimura, Keith Sweatman, Akira Kita, Shuhei Sawada, "A New Method of Increasing the Reliability of Lead-Free Solder," *Proceedings of SMTAI 2015*, 736-742, Rosemont, IL, October 2015.
49. A. Delhaise, L. Snugovsky, D. Perovic, P. Snugovsky, E. Kosiba, "The Effects of Bi and Ageing on the Microstructure and Mechanical Properties of Sn-rich Alloys, Pt. 2," *2016 International Conference on Soldering & Reliability*, Toronto, Canada, May 9-11, 2016.
50. David Witkin, "Mechanical Properties of Bi-containing Pb-Free Solders," *APEX Expo 2013*, San Diego, CA, February 16-21, 2013.
51. David Witkin, "Creep Behavior of Bi-Containing Lead-Free Solder Alloys," *Journal of Electronic Materials*, vol. 41, no. 2, 190-203, 2012.
52. David B. Witkin, "Influence of microstructure on quasi-static and dynamic mechanical properties of bismuth-containing lead-free solder alloys," *Materials Science and Engineering A*, vol. 532, 212-220, 2012.
53. André M. Delhaise, Polina Snugovsky, Ivan Matijevic, Jeff Kennedy, Marianne Romansky, David Hillman, David Adams, Stephan Meschter, Joseph Juarez, Milea Kammer, Ivan Straznicky, Leonid Snugovsky, Doug D. Perovic, "Thermal Preconditioning, Microstructure Restoration and Property Improvement in Bi-Containing Solder Alloys," *SMTA Journal*, vol. 31, issue1, 33-42, 2018.
54. Keith Sweatman, Nihon Superior, private communication, November 2017.
55. C. H. Raeder, L. E. Felton, D. B. Knott, G. B. Shmeelk and D. Lee, "Microstructural Evolution and Mechanical Properties of Sn-Bi based Solders," *Proceedings of International Electronics Manufacturing Technology Symposium*, 119-127, Santa Clara, CA, October 1993.
56. Richard Coyle, Raiyo Aspandiar, Michael Osterman, Charmaine Johnson, Richard Popowich, Richard Parker, Dave Hillman, "Thermal Cycle reliability of a Low Ag Ball Grid Array Assembled with Tin Bismuth Solder paste," *Proceedings of SMTAI*, 108-116, Rosemont, IL, September 17-21, 2017.
57. Richard Coyle, John Osenbach, Maurice Collins, Heather McCormick, Peter Read, Debra Fleming, Richard Popowich, Jeff Punch, Michael Reid, and Steven Kummerl, "Phenomenological Study of the Effect of Microstructural Evolution on the Thermal Fatigue Resistance of Pb-Free Solder Joints," *IEEE Trans. CPMT*, Vol. 1, No. 10, 1583- 1593, October 2011.
58. S. Terashima, Y. Kariya, Hosoi, and M. Tanaka, "Effect of Silver Content on Thermal Fatigue Life of Sn-xAg-0.5Cu Flip-Chip Interconnects," *J. Electron. Mater.* vol. 32, no. 12, 2003.
59. C. Lim et al, "Failure Characterization of BGA Solder Joint Fracture During Field Application," *12th Electronics Packaging Technology Conference*, December 2010.
60. Y. Mo et al "Failure Analysis on the BGA Solder Joint," *EEE Circuits and Systems International Conference on Testing and Diagnosis Conference*, 2009.
61. K. Sweatman, et al, "Reducing Cracking in Solder Joint Interfacial Cu6Sn5 with Modified Reflow Profile", *Transactions of The Japan Institute of Electronics Packaging* Vol. 13, 2020.
62. K. Sweatman, et al, "The Role of Nickel in Solder Alloys - Part 2. The Effect of Ni on the Integrity of the Interfacial Intermetallic in Sn-Based/Cu Substrate Solder Joints," *SMTAI Conference*, 2018.
63. D. Barbini, "Implementation of Lead-free Wave Soldering Process: An In-depth Look at the Critical Issues," *SMTA Pan Pacific Conference Proceedings*, 2005.
64. H. Manko, *Solders and Soldering*, ISBN 0-07-039970-0, McGraw Hill, 1992, 3rd Edition.
65. H. Schlessmann, "Lead-Free Technology and the Necessary Changes in Soldering Process and Machine Technology," *IPC APEX Conference Proceedings*, Session S4-01, 2002.
66. G. Diepstraten & H. Trip, "How to manage wave solder alloy contaminations," *IPC Midwest Conference presentation*, 2011.
67. Cookson Electronics, *CE Analysis Case Study #6*, On-line Report.
68. D. Hillman, et al, "JCAA/JG-PP No-Lead Solder Project: -55°C to +125°C Thermal Cycle Testing Final Report", *Rockwell Collins Working Paper WP06-2021*, October 2006.
69. Tin Whiskers: A History of Documented Electrical System Failures, A Briefing Prepared for the Space Shuttle Program Office, Dr. Henning Leidecker/NASA Goddard, Jay Brusse/QSS Group, Inc. April 2006.
70. Evaluation of Conformal Coatings for Future Spacecraft Applications, B.D. Dunn, European Space Agency document ESA SP1173, August 1994.
71. GEIA-STD-0005-2, Standard for Mitigating the Effects of Tin Whiskers in Aerospace and High Performance Electronic Systems, Section C.2.2.4 Conformal Coat or Foam Encapsulation Over Whisker Prone Surfaces, Government Electronics and Information Technology Association (GEIA), June 2006.

72. Website: <http://nepp.nasa.gov/WHISKER/experiment/exp2/index.html#current>.

73. Tin Whisker Risk Factors, David Pinsky, Michael Osterman, and Sanka Ganesan, IEEE Transaction on Components and Packaging Technologies, Vol. 27, No. 2, June 2004.

74. D. Hillman et al, "The Influence of Element Lead (Pb) Content in Tin Plating on Tin Whisker Initiation/Growth," Journal of SMT, Vol. 36, Issue 1, 2023.

75. ASM Metals Handbook, Metallography, Structures and Phase Diagrams, Volume 8, 8th Edition, 1973.

76. R. Klein Wassink, Soldering In Electronics, ISBN 0-901150-24-X, Electrochemical Publications Limited, 1989.

77. Milea Kammer/T. Pearson, private communication.



Richard Coyle is a Consulting Member of the Technical Staff in the Reliability Engineering organization of Nokia in Murray Hill, NJ. He is responsible for evaluating the reliability and quality of electronic assemblies in the Bell Labs Interconnection Failure Analysis Lab. He received his Ph.D. in Metallurgical Engineering and Materials Science from the University of Notre Dame. He is a member of TMS, ASM International, the EPS of IEEE, IMAPS, SMTA, and AWS. He is Co-Conference Director of SMTAI and a past member of the Board of Directors of SMTA (VP of Technical Programs). He is on the Board of Directors of iNEMI and an iNEMI Fellow.

BIOGRAPHIES



David D. Hillman is a Metallurgical Engineer in the Advanced Operations Engineering Department of Rockwell Collins Inc. in Cedar Rapids, Iowa. Mr. Hillman graduated from Iowa State University with a B.S. (1984) and M.S. (2001) in Material Science & Engineering. In his present assignment he serves as a consultant to manufacturing on material and processing problems. He served as a Subject Matter Expert (SME) for the Lead-free Manhattan Project in 2009. He has published 200+ technical papers. Mr. Hillman was named a Rockwell Collins Fellow in 2016. He was named an IPC Raymond E. Prichard Hall of Fame award recipient in 2018. He serves as the Chairman of the IPC JSTD-002 Solderability committee. Mr. Hillman served as a Metallurgical Engineer at the Convair Division of General Dynamics with responsibility in material testing and failure analysis prior to joining Rockwell. He is a member of the American Society for Metals (ASM), the Minerals, Metals & Materials Society (TMS), and Surface Mount Technology Association (SMTA) and the Institute for Interconnecting and Packaging of Electronic Circuits (IPC).



Tim Pearson is a Materials and Process Engineer in the Advanced Operations Engineering department of Collins Aerospace in Cedar Rapids, Iowa. Mr. Pearson graduated from Iowa State University with a BS in Materials Science and Engineering. Tim began his career as a Thin Films Engineer at Texas Instruments in a 300mm wafer fab. Tim has been working for Collins Aerospace (formerly Rockwell Collins) since 2015. In his current role, he helps develop new manufacturing processes, troubleshoots production issues, and does root cause analysis of failures related to soldering. He is a member of SMTA and IPC.

Vol 5 • Issue 1

2023

Signal Integrity

Signal Integrity • Power Integrity • EMC/EMI

Journal™

**GET YOUR
FREE
SUBSCRIPTION**

Get immediate access to:

- ▶ In-depth, Peer-Reviewed Technical Articles
- ▶ Insights from Industry Leaders
- ▶ Focused Reports
- ▶ Product & Industry News
- ▶ E-Learning Sessions
- ▶ Video Demos
- ▶ Print editions/technical e-books



SIGN UP ▶

Signalintegrityjournal.com/subscribe

Corporate Members

4Front Solutions	Analog Technologies Corporation	Checksum LLC	Dymax Corporation
AA Technology Inc.	ANDA TECHNOLOGIES USA INC	Cimetrix Incorporated	East West Wisconsin.
AAA Test Lab	Annapolis Micro Systems, Inc.	Circuit Works Corporation	EI Microcircuits
Abatek Americas Inc	Ansen Corporation	Cirtronics	EIS
AbelConn, LLC	Apollo Seiko	CO-AX Technology, Inc.	ELANTAS PDG, Inc.
Accu-Assembly Inc.	Appareo Systems	Cofactr Inc	Electronic Interconnect
Accu-Automation Corporation	Applicad Inc.	Colonial Electronic Manufacturers Inc.	Electronic Systems, Inc.
Accurate Technologies, Inc.	Aqueous Technologies	Comet X-Ray	Electronic Technologies International
ACDi	Arbell Electronics Inc	Comtree Inc.	Element Materials Technology Baltimore
ACL STATICIDE	ARCADIA TEST INC	Conductive Containers	Ellsworth Adhesives
actnano Inc.	Arc-Tronics, Inc.	Conesus Metals Conesus LLC	Eltek USA Inc.
ADCO Circuits, Inc.	Ascentec Engineering	Continental	Enercon
Advanced Component Testing	ASMPT SMT Solutions	Creation Technologies Inc.	Engent, Inc.
Aegis Software	ASYS Group Americas Inc.	Creative Electron, Inc.	EPTAC LLC
AI Technology, Inc.	Aven, Inc.	Critical Manufacturing	Esmartlink Technology Pte. Ltd.
AIM Solder	Axiom Electronics LLC	CRM Synergies	ESSEMTEC USA
Air-Vac Engineering	BBM, Inc.	Crown Equipment Corporation	Europlacer Americas
Akrometrix LLC	Berkshire Corp.	Cruise LLC	Express Manufacturing Inc.
Alert Tech SMT	BEST Inc.	Crystal Mark, Inc.	Facebook
All Flex Solutions	BGA Test & Technology	CSE	Fancort Industries, Inc
Allfavor Technology	Bittele Electronics Inc.	CTI Systems	FCT Assembly, Inc.
Alltemated	BlueRing Stencils	Cumberland Electronics Strategic Supply Solutions CE3S	Finetech
Alternative Manufacturing Inc.	Botron Company Inc	Cypress Technologies LP	Flex Mexico
Altronic, LLC (A Member of the Hoerbiger Group)	BPM Microsystems	Daktronics, Inc.	Flex USA
Amazon	Brady Corporation	Datest Corporation	FlexLink Systems, Inc.
American Hakko Products, Inc.	Braun Electronic Components	Datum Alloys	FTG Circuits Haverhill
American Standard Circuits, Inc.	BSE INC	DEKRA iST Reliability Services Inc.	Fuji America Corporation
American Technology Components Inc.	BTU International, Inc.	DELO Industrie Klebstoffe GmbH & Co. KGaA	Fusion EMS
Amitron Corporation	BTW Inc.	DG Marketing Corporation	GÄ-PEL electronic GmbH
Amphenol Borisch Technologies	Burton Industries, Inc.	Digital Audio Labs	Garland Service Company
	CalcuQuote	Divebiss Corporation	Garmin International
	Carel USA Inc.	Dorigo Systems Ltd.	GEN3 System
	Celestica, Inc.	Ducommun Incorporated	GHSP
	CEMSI		
	CeTaQ Americas		

Glenbrook Technologies Inc.	INVENTEC Performance Chemicals	Libra Industries, LLC	MOMENTIVE PERFORMANCE MATERIAL
Global Shop Solutions	IPS Assembly Corporation	Lockheed Martin	MSEI
GLOBAL SOLUTIONS ELECTRONICS	IPTE, LLC	Lunar Energy	MTE Solutions, Inc.
Google	iST-Integrated Service Technology Inc.	MacDermid Alpha Electronics Solutions	Murray Percival Company
Great Lakes Engineering	ITEC LATIN AMERICA	Mack Technologies Inc.	Musco Sports Lighting
Hanwha Techwin Automation Americas. Inc.	ITW Contamination Control	Magnalytix	Mycronic, Inc
Harman de Mexico S de RL de CV	ITW EAE	Maquiladora de Servicios MMS SA de CV	N.F. Smith & Associates, L.P.
Heller Industries	Jabil Circuit, Inc. (JDAS-STP)	MaRC Technologies	NAS Electronics
HISCOMEX	JAK ELECTRONICS LIMITED	Marco System Analysis and Development GmbH	National Instruments
Honeywell FM&T	Japan Unix	Master Bond Inc.	NCAB Group USA
HONG KONG LUK ELECTRONICS CO., LIMITED	JBC Tools USA Inc.	Matric LTD	Newtechnik Ind.Com.Prod.Eletr.Itda
Horizon Sales	JH Technologies	MBDA (UK)	Nihon Superior Company, Ltd.
Hughes Circuits, Inc.	John Deere Electronic Solutions, Inc.	MEK Americas	Nikon Metrology, Inc.
HumiSeal Europe Ltd.	Juki Automation Systems	MELECS Electronics Queretaro	Nokia Bell Labs
HZO	Juniper Networks	Metallic Resources, Inc.	Nordson Test & Inspection
I Source Technical Services, Inc.	KATEK Group	Metcal OK International	NPI Technologies, Inc.
iBtest	Keysight Technologies	MexSer	nScript
ICAPE USA	KIC	MG Chemicals	NSW Automation Sdn. Bhd.
IDENTCO	Kimball Electronics Inc.	Microboard	NVIDIA Corporation
IKEUCHI USA, INC.	Koh Young Technology Inc.	MicroCare Corporation	OmniOn Power
IMAT, Inc	Koki Solder America Inc.	Microchip	Omron Inspection Systems
Impossible Objects	kolb Cleaning Technology GmbH	Micron Corporation	PAC Global, Inc.
InCap Electronics US	Kostal Ireland GMBH	MicroScreen, LLC	PAC Mexico
Indium Corporation	Krypton Solutions	Microtech Laboratories LLC	PACE Worldwide
Ingenieria y Control Integral	Kulicke & Soffa PTE. LTD.	Mid America Taping and Reeling, Inc.	PalPilot International Corporation
Innovative Circuits, Inc.	KURTZ ERSÄ S.A. DE C.V.	Millennium Circuits Limited	Panasonic
Inovaxe Corporation	Kurtz Ersa, Inc.	Miller Electric Mfg. Co. - Components Division	PARMI USA INC.
Integrated Circuit Works	Kyowa Americas Inc.	Milwaukee Electronics	Partstack Corporation
Intel Corporation	KYZEN Corporation	Milwaukee Tool	PCB Connect Inc.
INTERFLUX	L3HARRIS	Mirac, LLC.	PCEA
Interlatin S. de R.L. de CV	LACROIX	Miraco, Incorporated	PDR Americas
Intervala, LLC.	LeeMAH Electronics, Inc.	Mirtec Corporation	PEMTRON CORPORATION
Intraratio Corporation	Lexicon Technologies Inc		Performance Review Institute
			Performance Technologies Group, Inc.

PFC Flexible Circuits	Restronics	SMT Union	Texmac/Takaya, Inc.
Pillarhouse USA, Inc.	Retronix	SMTto Engineering	The Jefferson Project
Pinnacle Technology Group	Rich Sales	SMTVYS LLC	The Test Connection, Inc.
Plato Systems	Rochester Institute of Technology (RIT)	SMTXTRA USA INC	Thermaltronics USA, Inc.
Plexus Corp.	ROCKA Solutions	SolderStar LLC	Time Way Electronics Limited
Polyonics, Inc.	Rockwell Automation	Solid Metals INC, DBA Solid Manufacturing	Tintronics
Powell Industries, Inc.	RTX / Raytheon Technologies	Southwest Research Institute	TouchPad Electronics LLC
PowerArena	Saki America Inc.	Space Dynamics Laboratory	Trans Tec America
Powertrain Control Solutions	Samtec	Spartronics	Transforming Technologies
PPSI	Saturn Electronics Corporation	Sparx Engineering	Transition Automation, Inc.
Practical Components	ScanCAD International, Inc.	SPEA America	Trenton Technology Inc.
Precision PCB Services, Inc.	SCHUNK Electronic Solutions	Specialized Coating Services	TT Electronics
Price Electronics	Schweitzer Engineering Labs	Specialty Coating Systems, Inc.	Unison Industries
PRIDE Industries	Scienscope	Spectrum AMT	Universal Instruments
Prime Technological Services	Securitas Healthcare	StaticStop a division of SelecTech, Inc.	Universal Scientific Industrial Co. Ltd.
Printed Circuits Corp.	SEHO North America, Inc.	StenTech, Inc.	Univertools
Pro-Active Engineering LLC	Seica Inc.	STI Electronics, Inc.	USM Reps
ProActive Process Solutions Group, LLC	Seika Machinery, Inc.	STIM Canada Inc.	Valtronic Technologies (USA) Inc.
Process Sciences, Inc.	Senju Comtek Corporation	Sunshine Global Circuits	Variosystems, Inc.
Production Automation Corporation	Sensible Micro Corporation	SVTronics, Inc.	VCount by Visiconsult X-ray Systems & Solutions GmbH
Projects Unlimited, Inc.	SHENMAO Technology, Inc.	Synapse Electronique Inc.	Venkel Ltd.
PROMATION USA	Shenzhen HTGD Intelligent Equipment Co., Ltd	Synco Corp	Versa Electronics
Promex Industries, Inc.	Shenzhen KHJ Technology Co.,Ltd	SynQor Inc	VEXOS
PVA	Shin-Etsu Silicones of America	Sypris Electronics, LLC	Virtual Industries Inc.
PVA TePla OKOS	Siborg Systems Inc	Tamura	Viscom
Quiptech	SICK, Inc.	Technica, USA	Vision Engineering
Rauland, A Division of Ametek	Signum, LLC	Technimark, Inc.	Vitrox Technologies Sdn. Bhd.
Raven Industries Inc.	Simco-Ion Technology Group	Techtron Systems Inc.	VJ Electronix, Inc.
Rawinski GmbH	SLB	Tecnova Electronics Inc.	VSE
RBB Systems	SMART Microsystems	Teknek	Watchfire Signs
Rehm Thermal Systems GmbH	Smart Splice, LLC	Teradyne, Inc.	Weller
Renishaw PLC	SMarTsol Technologies	Test Research, Inc.	Western Digital
Repstronics	SMT America	Test Technology Associates	West-Tech Materials, Inc.
Resources Unlimited Co. USA	SMT Resource Equipment	TESTEQUITY	

WIN SOURCE ELECTRONICS

WinTronics, Inc.

WORLD Electronics

XDry Corporation

X-Treme Series Auto Dry Cabinets

Yield Engineering Systems

Zapp Precision Strip

Zentech Manufacturing, Inc.

ZESTRON Corporation

Zollner Electronics Inc.

Zymet, Inc.



6600 City West Parkway, Suite 300
Eden Prairie, MN 55344 USA

Phone: +1-952-920-7682
Fax: +1-952-926-1819

E-Mail: smta@smta.org
Web site: www.smta.org

